Journal of Materials Chemistry A

ROYAL SOCIETY OF CHEMISTRY

REVIEW

View Article Online
View Journal | View Issue

Cite this: *J. Mater. Chem. A*, 2022, **10**, 4489

Iron-catalyzed graphitization for the synthesis of nanostructured graphitic carbons

R. D. Hunter,[a] J. Ramírez-Rico [b] and Z. Schnepp *[a]

Carbons are versatile and diverse materials that have numerous applications across energy and environmental sciences. Carbons with a graphitic structure are particularly appealing due to their high chemical stability, large surface areas and high thermal and electronic conductivity. Numerous methods exist to produce nanostructured graphitic carbons but some of these can be energy-intensive and/or have problems with scalability. One option that is being increasingly explored is the process of iron-catalyzed graphitization. This simply involves the pyrolysis of carbon-rich precursors in the presence of an iron catalyst and has been used to produce carbons with a wide range of structures and properties. This review will examine the current field of iron-catalyzed graphitization, with a focus on molecular organic or biomass precursors. Bio-derived precursors are particularly attractive as a potential option for sustainable production of graphitic carbons. We start with a brief introduction to some key carbon structures, the current applications in which they are employed and some of the key methods that have been developed to produce nanostructured graphitic carbons. We will then review the history of catalytic graphitization before evaluating the wide range of conditions and precursors that have been employed in catalytic graphitization. Finally, this review will investigate the current challenges facing iron-catalyzed graphitization, looking particularly at the limitations of the current understanding of the mechanistic aspects of graphitization, with a view to outlining where research in this field might progress.

Received 10th November 2021
Accepted 7th February 2022

DOI: 10.1039/d1ta09654k

rsc.li/materials-a

1. Introduction

Carbon has been at the heart of human technological development since the ancient discovery that metals could be extracted from rocks by heating them with charcoal (smelting). In the modern era, carbons find broad applications in energy and environmental applications as well as in pigments and as fillers for elastomers.[1] The value of carbon materials can be

[a]School of Chemistry, University of Birmingham, Birmingham, B152TT, UK. E-mail: z.schnepp@bham.ac.uk

[b]Dpto. Fisica de la Materia Condensada and Instituto de Ciencia de Materiales de Sevilla, Universidad de Sevilla-CSIC, 41092 Sevilla, Spain

Robert Hunter is currently studying for a PhD in the School of Chemistry at the University of Birmingham in the group of Dr Zoe Schnepp. His research is focused on the synthesis of porous graphitic carbons by iron-catalyzed graphitization of biomass-derived precursors. His work involves the use of both experimental and theoretical techniques to study mechanistic aspects of the graphitization process.

Joaquin Ramirez-Rico is a professor of Physics at the University of Sevilla, in Spain. He is the scientific director of the X-ray facility and heads a research group working on methods to convert biomass and natural resources into advanced materials for structural and functional applications. He was a Postdoctoral Fellow in Northwestern University and specialized in synchrotron radiation analysis for in situ characterization of materials. His current interests are in carbon materials for electrochemical energy storage and wastewater treatment.

evidenced by the fact that graphite is now classed as a critical material,[2] due to its importance in refractory materials and battery technology.[3] Many governments now recognise the need for future carbon materials to be sustainable, both for environmental concerns and economic security.

One class of carbon materials that is receiving increasing attention is that of nanostructured graphitic carbons. These boast a wide variety of useful properties that include high chemical stability, large accessible surface areas and high thermal and electronic conductivity. This makes graphitic carbon materials valuable in technologies such as batteries,[4] fuel cells[5] and in separation/purification science.[6] Numerous techniques have been developed to produce complex graphitic nanostructures, *e.g.*, chemical vapour deposition,[7] arc discharge,[8] or laser ablation[9] for the synthesis of carbon nanotubes. However, many of these methods are energy intensive and/or difficult to scale up. Therefore, there has been an international drive to develop cheaper, scalable, and more sustainable routes to nanostructured graphitic carbons.[10]

A promising method for the synthesis of nanostructured graphitic carbons is catalytic graphitization. Catalytic graphitization is broadly defined as the "transformation of non-graphitic carbon into graphite by heat treatment in the presence of certain metals or minerals".[11] The process normally occurs at a much lower temperature than graphitization without a catalyst, which makes it attractive from both an environmental and economic perspective. Various transition metals have been used to promote catalytic graphitization, but iron is particularly appealing, due to its abundance and low toxicity. Iron-catalyzed graphitization can be considered to include processes such as the production of graphite within blast furnaces or the chemical vapour deposition synthesis of carbon nanotubes. We will discuss these briefly, but the bulk of this article will describe the procedure of pyrolyzing mixtures of iron and organic precursors in an inert atmosphere to produce a range of nanostructured graphitic materials (Fig. 1). The simple conditions and wide range of potential organic precursors available for this process (including raw biomass) make it particularly appealing in terms of sustainability. We will compare the many examples of iron-catalyzed graphitization later in the review, but it is useful to start with a brief overview of carbon chemistry.

Zoe Schnepp is an Associate Professor in chemistry in the School of Chemistry at the University of Birmingham. Her research group is focussed on the synthesis of nanomaterials from biomass precursors, including ceramic nanostructures and porous carbons.

2. Carbon materials

2.1 Defining carbon structures

Defining (and naming) carbon materials is made challenging by the complexity and wide range of structures that are possible. Heating any organic material (synthetic or biological) in a low-oxygen atmosphere will generate a carbon-rich solid, with the chemistry and structure depending on the heating conditions and the nature of the precursor. Most of these carbon materials do not have a perfectly regular structure like that of diamond or graphite but instead are comprised of a mixture of features with significant variability and disorder. Considerable effort has gone into characterizing different types of carbon materials, for example through ^{13}C NMR spectroscopy,[12] Raman spectroscopy,[13] X-ray diffraction,[14,15] transmission electron microscopy,[16] total scattering,[17] electron energy loss spectroscopy (EELS) and X-ray photoelectron spectroscopy.[18] These techniques seek to probe features such as hybridization of the carbon atoms, the presence of sheet-like structures, interlayer spacing, orientation of stacked sheets, and sheet curvature caused by pentagonal or heptagonal rings of carbon. These materials are not just academic curiosities. Carbon blacks and activated carbons, for example, are widely used for air and water purification, as pigments in inks and as fillers in elastomers and plastics.[19] More recently, new carbon materials are also being developed for high-tech energy applications such as anodes for lithium and sodium batteries, where understanding of the fine structure is critical to optimizing their properties.[20–22]

Amorphous carbons are defined as containing a mixture of sp^2 and sp^3 hybridised carbon atoms and display no long-range crystalline order throughout their structure.[23] The surface of amorphous carbon typically consists of many reactive, dangling bonds,[24] and may also contain heteroatoms such as hydrogen, oxygen, nitrogen, or boron throughout the carbon network, depending on the method of synthesis. In contrast, graphitic carbons are composed of sp^2 hybridized carbon atoms arranged in hexagonal layers with long-range order that can be detected by diffraction methods. Strictly speaking, the term 'graphitic' should be reserved for carbon materials where the individual graphene layers are packed in an ABAB vertical arrangement.[25] However, many other carbon materials are commonly referred to as 'graphitic' if they have sheet-like structures arranged with an interplanar spacing similar to that of graphite. These can include multiwalled carbon nanotubes (Fig. 2a),[26] 'nanoscrolls',[27] bamboo-like carbon nanotubes (Fig. 2b),[28,29] which have a segmented structure, and onion-like carbons (Fig. 2c),[30–32] which consist of roughly spherical concentric layers of graphitic carbon surrounding a central 'core' that can either be hollow or contain a nanoparticle catalyst. Graphitic carbons have various appealing properties, including high electronic conductivity and chemical and thermal stability.[33] Another term that is commonly used in describing some carbon materials is 'turbostratic', derived from "turbo" (rotated) and "strata" (layer). Turbostratic carbons contain stacked sheets of

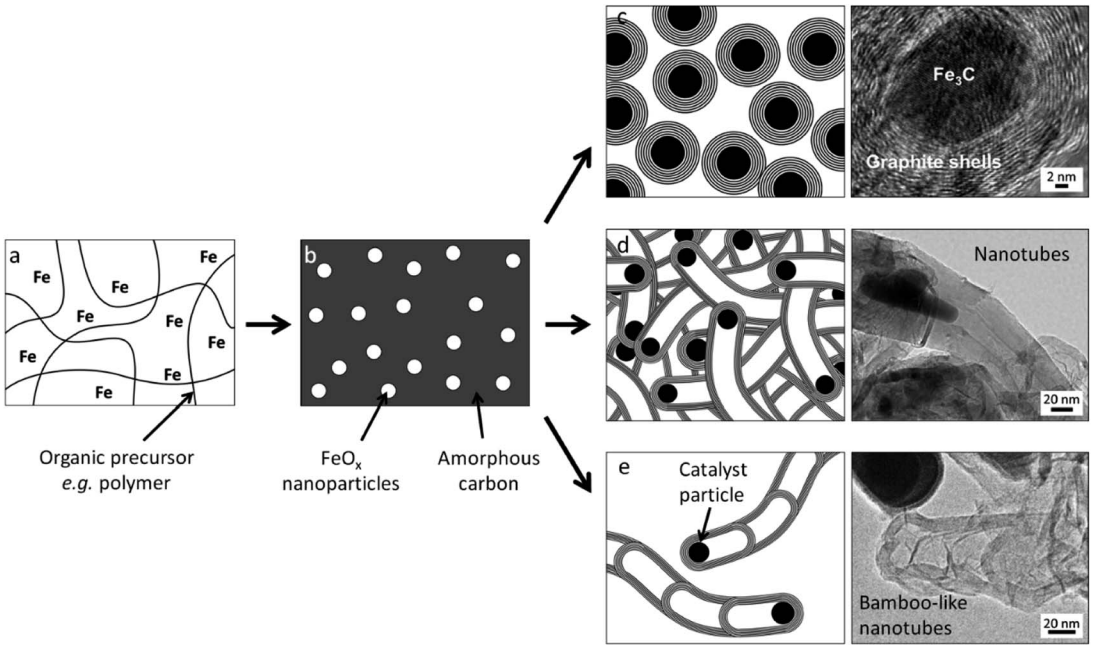

Fig. 1 Schematic of a typical iron-catalyzed graphitization process of pyrolyzing (a) an organic/iron mixture to initially produce (b) amorphous carbon and iron oxide nanoparticles then a variety of graphitic nanostructures such as (c) shells, (d) nanotubes and (e) bamboo-like nanotubes. Images reproduced with permissions from ref. 145 and 160.

sp^2-bonded carbon like graphite, but the sheets may exhibit random translation of the graphene layers along with rotational disorder, resulting in areas of larger interlayer spacing.[34] This can be observed in X-ray diffraction patterns as a broadening and/or a small shift to a lower 2θ value of the characteristic (002) peak.

An important factor in describing the chemistry of carbonization and carbon materials is the fact that some carbons resist graphitization. This was discovered in the early twentieth century and led to a seminal paper by Rosalind Franklin, who coined the terms 'graphitizing' and 'non-graphitizing' to describe different types of carbon.[35] She observed that some organic materials, such as polyvinylchloride and pitch, could be converted to crystalline graphite at >2200 °C whereas others, such as polyvinylidene chloride and sugar retain a porous isotropic structure even up to 3000 °C. Graphitizing and non-graphitizing carbons are commonly called 'soft' and 'hard' carbons, terms that relate to their observed physical properties. Understanding of the structure of hard and soft carbons has evolved with the development of increasingly sophisticated analytical techniques. The structures proposed by Franklin involved small crystallites of graphite, each of which contains several small graphene layers. In graphitizing carbons, these crystallites are approximately parallel to each other, facilitating graphitization (Fig. 3a). In non-graphitizing carbons, she proposed that the individual crystallites were crosslinked in a random orientation (Fig. 3b). More recent studies, using aberration-corrected TEM, ^{13}C NMR and total scattering, provide evidence for a 'fullerene-like' structure for microporous carbons, involving curved sheets of graphene arising from non-hexagonal carbon rings (Fig. 3c and d).[36–39] The structures of the different types of carbon are important as they may have

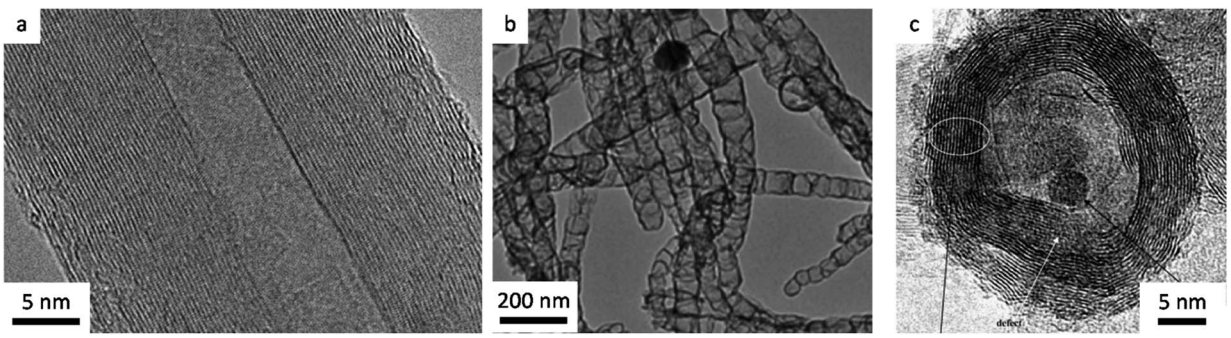

Fig. 2 Transmission electron microscope (TEM) images of (a) multiwalled carbon nanotube, (b) bamboo-like carbon nanotubes and (c) onion-like graphitic carbon shell. Images modified with permission from ref. 26, 29 and 31.

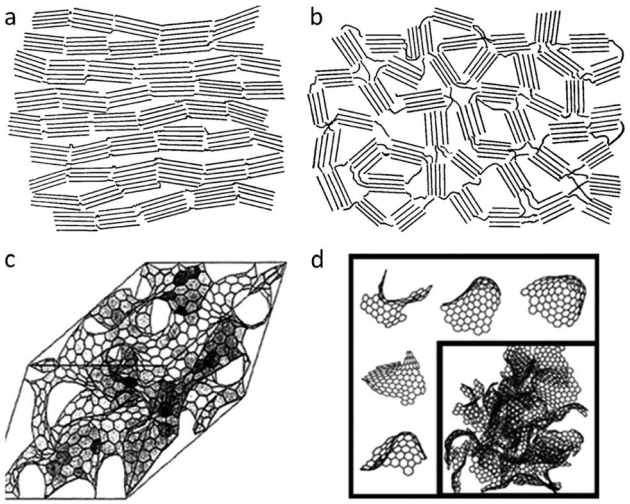

Fig. 3 Structures of (a) graphitizing and (b) non-graphitizing carbons proposed by R. Franklin. Also (c) curved graphitic sheet and (d) fullerene-like structural models of amorphous carbon. Images modified with permission from ref. 35, 38 and 39.

implications for the process of catalytic graphitization as well as helping us to describe and characterize some of the materials produced by catalytic graphitization.

2.2 Applications of carbon materials

As noted above, there are numerous applications for carbon materials and some of these represent large industries, for example the production of carbon black as a filler to improve the wear resistance of tyres.[40] Other significant industrial examples include carbon fibres for lightweight composites[41] and activated carbon for purification and environmental remediation.[42] It is outside of the scope of this article to cover all the applications of carbons and there are numerous reviews on the subject.[43–45] Instead, we will focus on several key applications that are the motivation of much of the work in the field of catalytic graphitization. These applications exploit the many useful properties of carbons produced by catalytic graphitization, such as porosity, electronic conductivity, chemical stability, and tuneable surface chemistry. Another driving force in this area is the potential for catalytic graphitization as a sustainable route to carbons since iron can produce graphitic structures at relatively low temperature (~800 °C).

One of the biggest areas of interest for carbons produced by catalytic graphitization is as electrocatalysts for the oxygen reduction reaction (ORR) in proton exchange membrane fuel cells.[46] The ORR occurs at the cathode, where oxygen is reduced by electrons and protons to produce water. This process commonly uses a noble-metal catalyst such as platinum, decorated on porous carbons. However, the cost and scarcity of noble-metals has led to a drive to find noble-metal free alternatives. Numerous authors have turned to functionalised carbons, many of which are produced by pyrolysis of organic species. This simple process can lead to a wide range of carbons, and it is possible to introduce various chemical and structural features to optimise catalytic activity. This can be achieved through the addition of iron species and by incorporating nitrogen functionality *via* the organic precursor or additives.[47] There are various potential ORR-active sites in Fe/N-doped carbons, such as Fe–N_x, N/C, and Fe_3C@C[48] and many of the materials rely on the beneficial properties of graphitic nanostructures (such as high electronic conductivity and thermal/chemical stability) that are produced during synthesis.

Pure graphite remains the material of choice for lithium-ion battery anodes as it displays excellent stability and reversibility.[49] However, natural and synthetic graphite both have limitations in terms of energy density, cost, and sustainability so there are considerable efforts to develop alternatives.[50] Catalytic graphitization offers a promising alternative and has been used to convert biomass into graphitic carbon materials that can be used in lithium-ion batteries.[51] The appeal of this method is that enables a relatively low processing temperature and the opportunity to use a renewable feedstock. Catalytic graphitization also has the advantage of being able to convert non-graphitizing carbons into graphitic structures. There are only a handful of examples of iron-catalyzed graphitization being used to produce materials for lithium-ion battery anodes but given the wide interest in using biomass as a precursor for this application,[52] it is likely to become a much larger area of research in the future.[53] It should be noted that there are also many efforts to produce nanostructured graphitic carbons for other energy storage applications such as sodium-ion batteries and supercapacitors.[54] The structural and chemical requirements for these applications are different and there are now many examples of carbons for energy storage produced by pyrolysis or catalytic graphitization of a range of precursors.[55,56]

A final promising application for nanostructured graphitic carbons is for use as adsorbents for separation or purification. As mentioned above, activated carbons are already used widely in industry for removal of various impurities or contaminants from air or water. Recently, many authors have investigated graphitic nanostructures such as carbon nanotubes and graphene for purification and separation applications.[57,58] There are various ways that graphitic features are believed to facilitate adsorption of contaminants, including π–π interactions with aromatic functionality of organic pollutants[59] or binding of heavy metal ions to defect sites or to tube ends.[60] Indeed, carbon nanostructures with significant sp^2 character such as nanotubes or graphene have been shown to have specific advantages over activated carbon.[61–63] However, the high cost of these specialist carbon materials limits their range of applications, particularly in environmental remediation.[64] Iron-catalyzed graphitization may offer an economical and sustainable solution, given the potential to transform bio-derived materials[65] or even waste biomass[66] into complex carbons with promising adsorption properties.

2.3 Production of carbon materials

This review focuses on the simple method of pyrolyzing organic molecules or materials with an iron precursor to generate graphitic carbon nanostructures. However, it is useful to give

a brief overview of other approaches to synthesizing carbon materials as studying them can offer insight into the mechanism of iron-catalyzed graphitization. The first known production of carbon materials dates to the paleolithic era, where early humans used charcoal for cave paintings.[67] Charcoal was made in simple earth-covered kilns, where wood is slowly burned with a limited supply of air. The development of charcoal is tied to the discovery of metal smelting.[68] Charcoal fires burn much hotter than wood fires, which are limited by the release of significant amounts of water and volatiles. The heat and reductive environment of a charcoal fire is what facilitates the extraction of metals from their ores. Charcoal has endured as a useful material to humankind due to its ease of production and high purity compared to coal and coke.[69] Many modern carbon materials are produced using technology that is fundamentally very similar to that of ancient charcoal kilns *i.e.* pyrolysis of organic matter in a low-air environment. However, modern furnaces enable much better control over heating conditions and purity of atmosphere. The main factor affecting the properties of the resulting carbon is the nature of the organic precursor. For example, carbon black is a fine powder with high surface area and electronic conductivity that is typically produced by the reaction of hydrocarbon fuels with a limited supply of air.[19] In contrast, biochars are produced by the pyrolysis of biomass in the absence of oxygen and tend to maintain the macrostructure of the biomass source.[70] Biochars have reasonably high porosity but carbons that are produced by pyrolysis of solid materials can gain higher porosity through 'activation'. This can be achieved through chemical (*e.g.* phosphoric acid, sodium hydroxide or zinc chloride) or physical (*e.g.* steam) treatment of the char.[71]

Carbon black and activated carbon are two of the most industrially important carbon materials but there have been substantial efforts to develop routes to more specialist carbon materials such as fullerenes or nanotubes. One of the earliest examples is arc discharge. In this method, an electrical arc between two electrodes in a non-conductive gas is used to generate a plasma. The high-temperature plasma vaporizes solid graphite from the anode, which then deposits onto the cooled cathode as structures such as carbon nanotubes[72] and fullerenes.[73] The graphite anode can be doped with various metals such as nickel, iron or cobalt, which act as catalysts for the growth of nanotubes and can facilitate growth of specific structures such as single or double-walled carbon nanotubes.[74] Arc-discharge continues to be an area of interest for many researchers[75] and there is still much to be learned about graphitization in this system, but that is outside the scope of this review. Another technique for growing carbon nanotubes is laser ablation, which was developed to create more controllable conditions. Laser ablation was first reported by Guo *et al.*,[9] and uses a pulsed laser beam to vaporize a graphite target with embedded metal catalyst particles. Like arc discharge, the resulting carbon vapour is deposited onto a cooled substrate in the form of nanotubes and fullerenes.[76]

Arc-discharge and laser ablation both require a lot of energy and are difficult to scale up. As a result, an alternative method called chemical vapour deposition (CVD) was developed to facilitate the industrial manufacture of carbon nanotubes. In addition to the lower energy requirements, CVD has the advantage of not requiring pure graphite as a reagent. Instead, a gaseous hydrocarbon such as acetylene flows over a two-dimensional substrate. The substrate is coated in nanoparticles of a metal catalyst (typically iron, cobalt, or nickel) and when the hydrocarbon gas is heated, it decomposes and dissolves into the catalyst. Carbon nanostructures grow from the catalyst nanoparticles by various mechanisms such as float growth or base growth (Fig. 4). Compared to arc discharge and laser ablation, CVD can produce a relatively high purity product in a high yield. By changing various experimental parameters such as reaction temperature or the chemical nature of the catalyst or substrate, it is possible to influence the structure of the final product and CVD methods are widely used in industrial manufacture of carbon nanostructures. It is worth noting that many of the methods discussed in this section employ transition metal catalysts such as nickel, cobalt or iron. Considerable effort has gone into elucidating the mechanism by which these catalysts produce carbon nanostructures. While the conditions of iron-catalyzed graphitization are very different from those of arc discharge, laser ablation and CVD, there is much we can learn from the extensive mechanistic studies of these processes, and we will return to this later in the review.

3. A brief history of catalytic graphitization

Humankind has been exploiting catalytic graphitization for thousands of years, long before the technology evolved for us to understand the chemistry. For example, pottery from an ancient settlement called Keeladi in India has a durable black coating that was found to be made up of multi-walled carbon nanotubes.[77] These are believed to have been formed during firing from carbonization of plant matter alongside naturally occurring catalytic iron species. In another example, ancient Damascus steel blades, renowned for their strength and sharpness, have shown a complex microstructure of carbon nanotubes and iron carbide nanowires.[78] Catalytic graphitization by iron may even occur naturally throughout the universe, with evidence

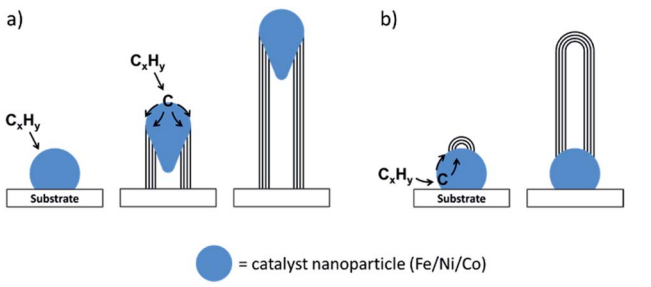

Fig. 4 (a) Float growth and (b) base growth mechanisms of carbon nanotube growth in chemical vapour deposition, driven by decomposition of a hydrocarbon gas and dissolution of carbon into a catalyst particle.

that iron has driven the formation of graphitic structures found on meteorites.[79]

In more recent years, there have been more deliberate efforts to understand and exploit the process of catalytic graphitization. Many of these have stemmed from an interest in improving the efficiency of graphite production by reducing the typical synthesis temperature of >3000 °C.[80] The ability of 'impurities' to drive catalytic graphitization at much lower temperatures was discovered by Acheson[81] in 1896. Since then, many different elements and alloys have been shown to promote the transformation of amorphous carbon to graphitic carbon.[82] Early attempts involved the pyrolysis of mixtures of metal powders with amorphous carbons.[83] The differences in the type of carbons formed (graphitic or turbostratic/graphitic) were linked to two different graphitization mechanisms. The first of these was proposed to be formation and subsequent decomposition of metal carbides and the second was suggested to involve dissolution of carbon into the catalyst, followed by reprecipitation.[84] The latter mechanism was believed to be driven by formation of a solution that is saturated with respect to disordered carbon but supersaturated with respect to graphite.[85,86] The precise composition of the carbon precursor was found to affect the degree of graphitization, but importantly, it was shown that even 'non-graphitizable' carbons could be graphitized at relatively low temperatures (<1400 °C).[87]

The specific phenomenon of iron-catalyzed graphitization has been studied in considerable detail since the early reports of catalytic graphitization. This is partly due to the importance of graphitization within the iron and steel industry. For example, in blast furnaces, iron ore is heated with a porous carbon such as coke, which acts as a reducing agent and energy source and is also crucial in maintaining the permeability of the reactor contents for upward flowing gases.[88] For environmental reasons, there is a need to minimize coke consumption, which has driven investigations into coke degradation and transformation within blast furnaces.[89] One mechanism by which this occurs is the graphitization of coke carbon. A model study used to probe this system combined coke with a fine iron powder (particle size <5 μm). Heating the mixture resulted in the formation of graphitic carbon above 1200 °C.[90] The process is believed to result from a dissolution–precipitation mechanism within molten iron catalyst particles.

Another observation that prompted study into iron-catalyzed graphitization was the unwanted deposition of carbon on metals exposed to carbon monoxide. For example, the conversion of carbon monoxide to solid carbon on iron surfaces was observed to cause deactivation of Fischer–Tropsch catalysts,[91] damage to brickwork in blast furnaces,[92] and carburization in heat exchangers of nuclear reactors.[93] While carbon deposition can be problematic in these circumstances, it was recognised that the same process may enable industrial production of useful carbons. In studying carbon deposition, many authors observed tube like filaments, with small crystals of iron or iron carbide (Fe_3C), indicating that the iron had catalyzed the filament formation. Work quickly moved to the deliberate synthesis of these tubular filaments from decomposition of carbon monoxide[94] or benzene[95] over iron catalysts. This research led to development of CVD synthesis of carbon nanotubes,[96] as discussed above.

Alongside development of gaseous precursors for catalytic graphitization, there has been increasing interest in iron-catalyzed graphitization of non-gaseous organic precursors. This typically involves mixing solvated iron precursors such as ferrocene, iron nitrate, iron acetate or iron chloride with a solid or dissolved organic material.[83,97,98] The mixture is then pyrolyzed in an inert atmosphere to drive thermal decomposition of the organic matter to amorphous carbon. Alongside this, the iron precursor also decomposes. In many cases this results firstly in iron oxide nanoparticles, which are then transformed by carbothermal reduction to Fe or Fe_3C. These particles then drive graphitization, which is believed to occur either by dissolution/reprecipitation of carbon or formation/decomposition of carbides. Due to the relatively small size of the catalytic iron nanoparticles, the graphitization process occurs at the relatively low temperature of 800 °C or 900 °C. In many instances, tubular nanostructures are formed, suggesting that the iron-containing catalyst particles move through the amorphous carbon matrix during graphitization, perhaps driven by dissolution and reprecipitation of carbon. Multiple variations of this procedure now exist, using a wide range of organic precursors and these will form the basis of the next sections of this review. We will then return to the question of the mechanism of graphitization.

4. Organic precursors used in iron-catalyzed graphitization

This section will present the main categories of organic precursors that have been used in iron-catalyzed graphitization. A few examples from the literature will be discussed to highlight the diversity of the method, focusing particularly on those in which effort has been made to explain or influence the formation of the graphitic carbon product.

4.1 Small organic molecules

The simplest organic precursors used in iron-catalyzed graphitization are small molecules such as sucrose and glucose. These sugars are highly soluble in water so can be combined with aqueous iron salts such as iron(III) nitrate to produce a homogeneous solution or gel. This is then dried and pyrolyzed to yield graphitic carbon structures (Fig. 5a). An example of this can be seen in the work of Yang *et al.*, who synthesized graphitic shell-like structures containing metal particles by pyrolyzing a mixture of sucrose and iron(III) nitrate above 700 °C (Fig. 6a).[99] The metal nanoparticles can be removed by acid-washing to leave graphitic "capsules" (Fig. 6b), alongside a smaller number of graphitic nanotubes, highlighting the possibility of the formation of different nanostructures within the same product. Sevilla *et al.* found that a combination of iron nitrate and glucose could be used to produce filamentous multi-walled nanotubes, suggesting that the catalyst in this system is highly mobile (Fig. 6c and d).[100] It is difficult to know whether sucrose and glucose themselves influence the process of

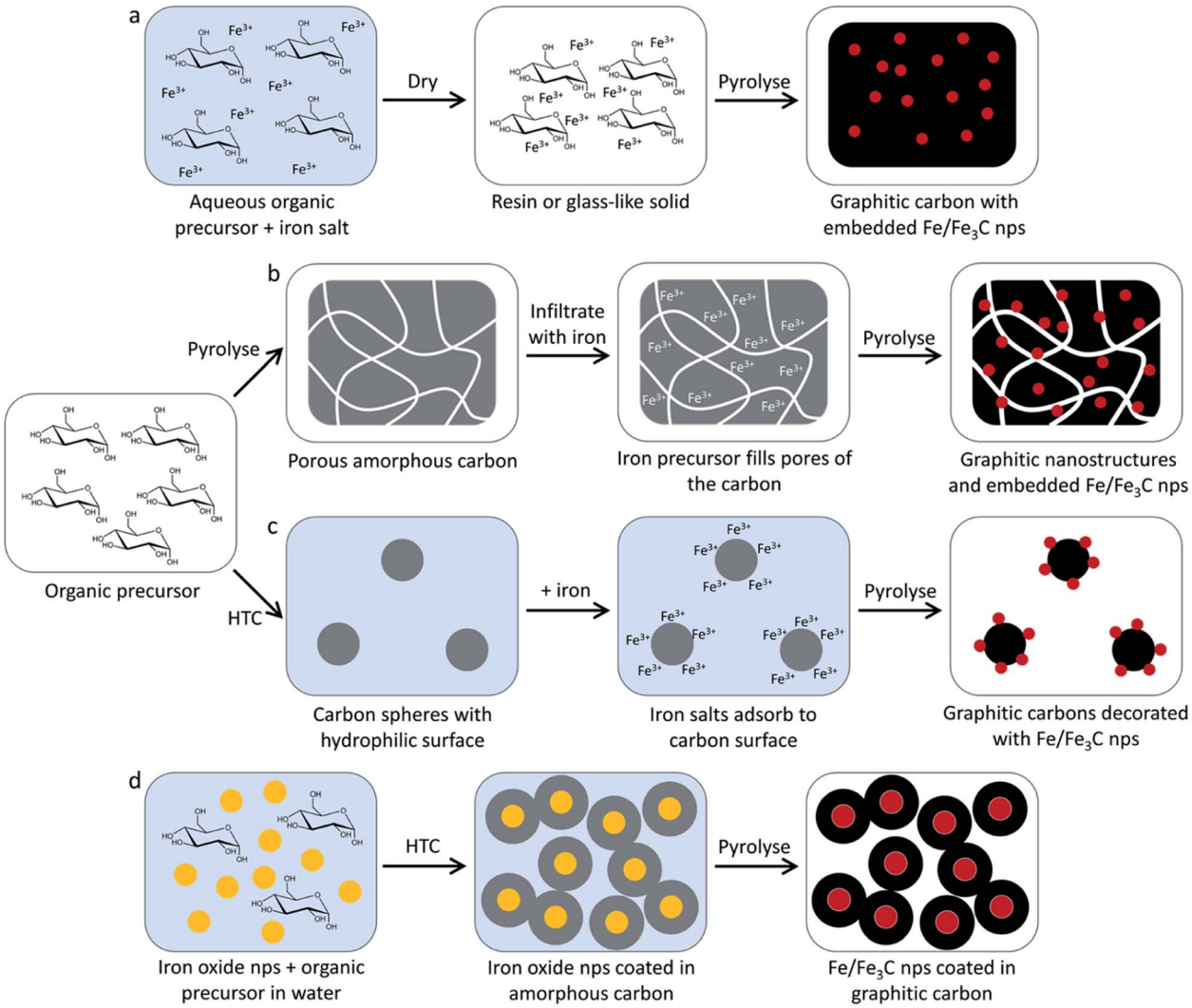

Fig. 5 Schematic showing some of the methods that have been used to prepare nanostructured graphitic carbons from small organic molecule precursors such as glucose. These include (a) simple pyrolysis of a mixture of the organic precursor with an iron salt, (b) pyrolysis of the organic precursor followed by infiltration with an iron salt and a second pyrolysis step, (c) hydrothermal carbonization (HTC) followed by adsorption of iron species onto the resulting carbon spheres and (d) hydrothermal carbonization around iron oxide nanoparticles, followed by pyrolysis.

graphitization as the metal : organic ratio and heating conditions are quite different in these two papers. Also, the sucrose was mixed with iron nitrate in water, whereas the glucose system employed ethanol as a solvent. It seems most likely, however, that the metal : organic ratio is the dominant reason for the difference in these systems. The 'shell' like structures

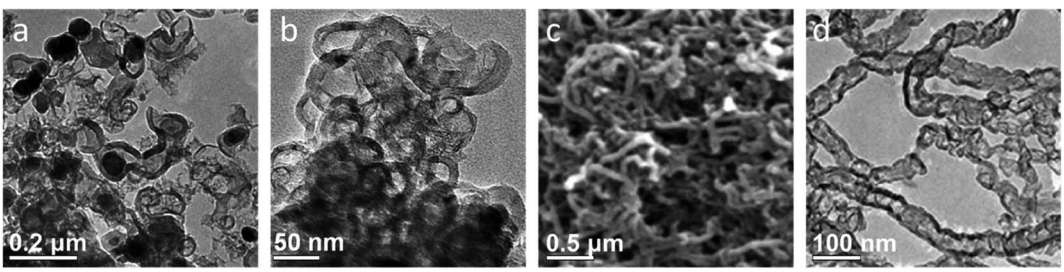

Fig. 6 TEM images of (a) graphitic nanostructures with embedded iron nanoparticles produced by pyrolyzing a mixture of sucrose and iron nitrate and (b) the same sample after acid-washing. (c) Scanning electron microscope (SEM) and (d) TEM images of graphitic nanotubes produced from glucose and iron nitrate (after acid washing to remove iron catalyst particles). Figures modified with permission from ref. 99 and 100.

were produced from a system containing 3 millimoles of iron per gram of sucrose and the nanotubes came from mixtures of 0.4 or 0.8 millimoles of iron per gram of glucose. The glucose system would therefore have a lot more amorphous carbon available, which could allow for substantial movement of the catalyst particles during catalytic graphitization before all the carbon is consumed. In a further example using aqueous glucose and iron nitrate, shell-like structures were observed rather than nanotubes.[101] Again, it is difficult to conclude anything about the mechanism as the authors also used NaCl as a sacrificial template but the ratio of 1.7 millimoles of iron per gram of glucose is similar to the levels used by Yang *et al.* to produce shell-like structures. This lends credence to the argument that the metal : organic ratio is most important in dictating the type of structures formed in these systems. Another study that used sucrose, glucose and urea with iron acetylacetonate showed that all organic precursors resulted in carbons that show a mixture of shell-like and short tubular structures.[102] Some differences were observed in the iron/iron carbide composition and the graphite peak height in XRD but the suggestion overall is that iron : organic ratio has a more significant impact on graphitization than the chemistry of the different small-molecule precursors.

Sugars have also been used to produce carbons where graphitic nanostructures are combined with macrostructural features such as pores or spherical shapes. The simplest approach to this is to initially produce an amorphous carbon and then introduce iron before pyrolyzing (Fig. 5b). This can be achieved just by pyrolyzing a sugar such as glucose to produce a porous amorphous carbon,[103] but more elaborate structures can be formed by templating sugars with amphiphilic copolymers before carbonizing them.[104] In the copolymer-templated example, the resulting amorphous carbon was then decorated with iron oxide nanoparticles by hydrothermal treatment and then pyrolyzed a second time to drive graphitization. Hydrothermal chemistry can also be used to produce the amorphous carbon precursor *e.g. via* hydrothermal carbonization of sucrose solutions to generate carbon spheres. The surface of these can be impregnated with iron nitrate, followed by pyrolysis to generate carbon spheres with a highly graphitic surface (Fig. 5c).[105] Hydrothermal carbonization can also be used to deposit carbon from glucose around iron oxide nanoparticles before pyrolysis to drive graphitization (Fig. 5d). This has the advantage of maintaining a relatively consistent catalyst particle size.[106] It is not particularly instructive to continue discussing all examples of iron-catalyzed graphitization that employ small molecules. A selection of examples from the literature are listed in Table 1 and it can easily be seen that a wide range of precursors and conditions have been used, even within this small area focusing on small molecules. It is clear from these examples that there is scope for tailoring graphitic nanostructures even in very simple systems but there is a need for systematic investigation.

4.2 Synthetic polymers

A large range of synthetic polymers have been used as precursors for graphitic carbons and these are summarized in Table 2. As with small organic molecule precursors, the simplest way to produce graphitic carbons from synthetic polymers is to produce a homogeneous mixture of the polymer with an iron compound and pyrolyze in an inert atmosphere. For example, Huang *et al.* produced bamboo-like hollow carbon fibres from an aqueous mixture of polyethylene glycol and iron sulfate.[116] Interestingly, these authors found that the carbon nanofibre yield decreased with a high iron loading, suggesting that catalyst particle size may be important in regulating graphitization. Rather than mixing an iron precursor directly with the polymer, it is also possible to mix the iron precursor with a monomer and then initiate polymerization, before pyrolyzing the resulting material. This method has been used to produce graphitic carbon nanostructures from polyfurfuryl alcohol. It should be noted that the structures produced in these systems are turbostratic (*i.e.* no regular stacking between layers) rather than truly graphitic, as indicated by an absence of *hkl* diffraction in selected area electron diffraction (SAED) studies.[97] This is probably true of most of the examples in this section but is typically not stated by authors.

A common type of synthetic polymer used for catalytic graphitization is phenolic resins. These are thermosetting polymers that are generally synthesized from the reaction of phenols with formaldehyde and are commonly used as industrial adhesives. The type of structures and porosity of graphitic carbons produced from phenolic resins depends on the type of iron precursor (*e.g.* iron nitrate or ferrocene)[117] and also the method of mixing, with mechanical mixing of solid precursors favouring micropores and homogeneous mixing of solvated precursors favouring mesopores.[118] This is due to the homogeneously-mixed sample displaying more graphitic features, compared to the micropores of amorphous carbon. Organic gels formed from the reaction between resorcinol and formaldehyde have also been successfully graphitized by iron-based catalysts. Again, the polymerization is performed in the presence of the iron precursor, allowing a homogeneous mixture of the two components. An interesting example by Hasegawa *et al.* uses resorcinol, iron chloride and formaldehyde in an ethanol/water solvent.[119] The iron chloride acts as an acid catalyst to initiate polymerization and as the reaction proceeds, the polymer network becomes more hydrophobic, leading to spinodal decomposition and the formation of a macroporous structure. The pore size can be controlled simply by varying the ethanol:water ratio and the macroporosity is maintained in the graphitic product after pyrolysis (Fig. 7a).

Another route to introduce porosity into graphitic carbons produced from synthetic polymers is to use hard or soft templates. These can be sacrificial or can themselves form part of the carbon product or the catalyst. Maksimova *et al.*,[120] embedded needle-shaped iron hydroxide nanoparticles in polyvinylalcohol and polyethylene before pyrolysis under nitrogen. TEM images of samples heated to 600 °C showed needle-like iron oxide crystals (from iron hydroxide decomposition) coated in a layer of amorphous carbon (Fig. 7b). Pyrolysis to 750 °C results in carbothermal reduction of the iron oxide to iron and a markedly different structure (Fig. 7c) where the carbon has retained the needle-like structure but the catalyst

Table 1 List of examples of graphitic nanostructures produced from small molecule organic precursors

Product description	Organic precursor	Iron source	Temp. (°C)	Notes	Catalyst
Graphitic tubes/shells[108]	Glucose	$Fe(NO_3)_3$	800	BET surface area 343 $m^2 g^{-1}$	Fe_3C
Graphite[103]	Glucose	Fe powder	1200	Glucose pyrolysed to form hard carbon before grinding with iron powder	
Carbon-encapsulated magnetic nanoparticles, core–shell structure[106]	Glucose	Fe_3O_4 nanoparticles	700–850	BET surface area 134–202 $m^2 g^{-1}$	
Graphene-like carbon shell encapsulating iron carbide nanoparticles[107]	Glucose	$Fe(NO_3)_3$	800	Potassium nitrate added as a promoter, BET surface area 238 $m^2 g^{-1}$	Fe_3C
Mesoporous graphitic carbon[108]	Glucose	$Fe(NO_3)_3$	800	Comparison with starch and cellulose BET surface area 343 $m^2 g^{-1}$	Fe_3C
Graphitic mesoporous carbon, carbon nanotubes[99]	Sucrose	$Fe(NO_3)_3$	700/800	BET surface area 198 $m^2 g^{-1}$	
Nanoporous graphitic carbon, wormlike porous structure[104]	Sucrose	$Fe(NO_3)_3$	600–900	Initial hydrothermal treatment, F123 copolymer template, BET surface area 329 $m^2 g^{-1}$	
Graphitic nanoribbons[105]	Sucrose	$Fe(NO_3)_3$	800	Initial hydrothermal treatment	
Hollow carbon nanospheres[109]	Sucrose	Iron oxide nanoparticles	450	Very broad peak in XRD	Fe_3C
Fe_3C or Fe nanoparticles with graphitic shells[102]	Glucose, sucrose, or urea	Iron acetylacetonate	800	BET surface area 40–240 $m^2 g^{-1}$	Fe_3C or Fe
Graphite encapsulated iron carbide/iron nanosheet composites[110]	Glucose and glycine	$Fe(NO_3)_3$	700–1000	BET surface area 75–260 $m^2 g^{-1}$	Fe_3C then Fe
Iron particles with graphitic carbon shells[111]	Glucose + dicyandiamide or urea	$K_3[Fe(CN)_6]$	800/900	NaCl template, dicyandiamide or urea for N-doping	Fe/Fe_3C
Iron and nitrogen doped carbon nanostructures[112]	Glycine	$FeCl_2$	900	Additional template of silica beads, BET surface area 740 $m^2 g^{-1}$	
Iron-doped porous carbon, graphene sheets, particles wrapped by graphitic carbon[113]	L-Histidine	Fe_2O_3 and $FeCl_3$	1000 then 1000	Ball milling and acid wash after first pyrolysis, BET surface area 200–315 $m^2 g^{-1}$	
Metallic nanoparticles in graphitic shells[114]	Citric acid	$Fe(NO_3)_3$	800	Initial formation of metal citrate gel at 120 °C	
Iron carbide encapsulated in graphitic layers[115]	1,8-Diaminonaphthalene	$FeCl_3$	700–1000	Initial polymerisation step, BET surface area 510–920 $m^2 g^{-1}$	Fe_3C

particles have moved out of the carbon shells to form much larger, rounded particles. This suggests that the catalyst phase is highly mobile and the authors propose that this indicates a melting transition of the catalyst particles. Sevilla *et al.* produced mesoporous carbons by impregnating silica xerogels with a solution of phenolic resin in methanol, followed by pyrolysis and etching of the silica template with HF.[121] The resulting mesoporous carbons were then filled with ethanolic iron nitrate and pyrolyzed to 400–900 °C before removing the metal catalyst particles by acid washing. The combination of graphitic features and porosity from the silica template led to remarkably high surface areas and bimodal porosity. Interestingly, these authors found that a lower pyrolysis temperature (≤600 °C) favoured graphitization, perhaps because high temperatures drove sintering of the catalyst particles. In a similar method, Li *et al.* synthesized a mesoporous silica template (Fig. 7d) with embedded iron oxide particles that was infiltrated with phenolic resin, pyrolyzed at 900 °C and washed with HF to generate a mesoporous graphitic carbon (Fig. 7e).[122]

The challenge with using silica as a template is the need for harsh treatment (HF or strong NaOH) to remove the silica. An alternative approach is to use soft templates which can be combusted during the pyrolysis process. For example, Wang *et al.* used Pluronic P123 to introduce mesoporosity into a phenolic resin.[123] Pyrolysis without iron produced a carbon with regular porosity and a high surface area of 800 $m^2 g^{-1}$. However, much of this ordered porosity appears to be lost if an iron precursor is also included in the phenolic resin, with the formation of graphitic nanostructures and a lower BET surface area. Another system showed more successful retention of ordered mesoporosity. Li *et al.* employed a triblock copolymer Pluronic F127 to produce resorcinol-formaldehyde resins with ordered mesoporosity.[124] They discovered that a high iron content led to loss of the ordered porosity but that it could be maintained at a low iron:organic ratio (Fig. 7f), with metallic iron nanoparticles dispersed throughout the structure.

4.3 Biopolymers

Polymers derived from biomass (often called biopolymers) offer an attractive alternative to synthetic polymers as they are renewable and could therefore offer a sustainable route to materials. Many biopolymers may also be waste products of industrial processes so producing graphitic carbons may be a way to add value to unwanted materials. In this section, we will consider both soluble and insoluble biopolymers as it is

Table 2 List of graphitic nanostructures produced from synthetic polymers

Product description	Organic precursor	Iron source	Temp. (°C)	Comments
Turbostratic carbon shells and tubes surrounding Fe nanoparticles[97]	Furfuryl alcohol	Ferrocene	450–820	Initial polymerization step to polyfurfuryl alcohol
Turbostratic carbon, shell-like structures[125]	Furfuryl alcohol	Ferrocene	700	BET surface area 200 $m^2 g^{-1}$
Graphitic mesoporous carbons[121]	Phenolic resin	$Fe(NO_3)_3$	900	Silica xerogel template, BET surface area 1010 $m^2 g^{-1}$
Graphitic mesoporous carbon[117]	Phenolic resin	$Fe(NO_3)_3$ or ferrocene	700	BET surface areas of 607 $m^2 g^{-1}$ and 248 $m^2 g^{-1}$
Onion-like carbon[126]	Phenol/ formaldehyde	Ferrocene	1000	Different mixing methods compared
Microporous carbons, graphitic layers[118]	Phenol/ formaldehyde	Ferrocene	1000	Mechanical mixing compared to solution mixing, BET surface areas 216–632 $m^2 g^{-1}$
Mesoporous carbon[122]	Phenol/ formaldehyde resin	$Fe(NO_3)_3$	900	SBA-15 silica nanocast BET surface area 670 $m^2 g^{-1}$
Mesoporous graphite-like carbon[123]	Phenol/ formaldehyde	Ammonium iron citrate	700	Pluronic P123 as templating agent
Ordered mesoporous carbons with partially graphitized network[127]	Phenol/ formaldehyde	$FeCl_3/FeSO_4$	800	Initial hydrothermal treatment and copolymer P123
Graphitic mesoporous carbon[128]	Resorcinol/ formaldehyde	Iron citrate	900	Silica sol template, surface area depends on iron content
Highly ordered Fe-containing mesoporous carbon[124]	Resorcinol/ formaldehyde	$Fe(NO_3)_3$	800	Triblock copolymer pluronic F127 templating agent
Metal-doped carbon aerogels[129]	Resorcinol/ formaldehyde	Iron acetate	900	BET surface area 461 $m^2 g^{-1}$
Graphitic carbon spheres[130]	Resorcinol/ formaldehyde spheres	Prussian blue	1000	BET surface area 381 $m^2 g^{-1}$
Macroporous monolithic graphitic carbon[119]	Resorcinol/ formaldehyde xerogel	$FeCl_3$	1000	Spinodal decomposition during polymerization introduces macroporosity, BET surface area 465 $m^2 g^{-1}$
Onion-like or nanocapsule-like graphitic carbon[131]	Resorcinol/ formaldehyde	Iron(II) acetate	1100	Two step pyrolysis to minimise cracking
Monolithic porous graphitic carbons[132]	Resorcinol, furfural xerogel	$FeCl_3$	1050	BET surface areas up to 400 $m^2 g^{-1}$
Carbon nanotubes and shells[120]	Polyethylene/ polyvinyl alcohol	Iron hydroxide needles	750	
Carbon nanofibers with bamboo-like hollow fibril morphology[116]	Polyethylene glycol	$FeSO_4$	750	Graphitization believed to be facilitated by sulfur dissolution into the catalyst particles
Carbon nanotubes[133]	Polypropylene	Fe nanoparticles	700	Dissolution of precursor in xylene
Multilayer graphitic nanosheets/ nanoshells[134]	Poly(4-ethylstyrene-*co*-divinylbenzene)	Iron(II) acetylacetonate	850	

instructive to do so, and some may 'swell' rather than truly dissolve. In the following section we will discuss raw biomass. A summary of biopolymer-derived graphitic carbons can be found in Table 3.

The most abundant biopolymer found in nature is cellulose, which is the main component in the cell walls of green plants. Cellulose is a polysaccharide consisting of linear chains of $\beta(1\rightarrow4)$ linked glucose units. Cellulose molecules align to form strong microfibrils, with individual cellulose polymers bound together by hydrogen bonds and it is networks and arrays of these microfibrils that provides much of the mechanical strength of plants. Cellulose can be extracted from plant material (or from cellulose-producing bacteria) but is very difficult to solubilise, requiring specialist conditions such as ionic liquids[135] or concentrated NaOH at controlled temperatures[136] to be dissolved. All the examples of iron-catalyzed graphitization of cellulose therefore use pure solid forms of cellulose such as fibres or microcrystalline powders.

A range of iron precursors have been used for catalytic graphitization of cellulose. Hoekstra *et al.* pyrolyzed microcrystalline cellulose spheres impregnated with three trivalent iron salts: iron(III) nitrate, ammonium iron(III) citrate and iron(III) chloride.[65] The study showed several interesting results. X-ray diffraction of all three systems showed similar compositions in the resulting carbons, with peaks for Fe and Fe_3C and a broad peak corresponding to the interlayer plane spacing of graphite. However, only the iron nitrate and ammonium iron citrate showed the shell-like and tube-like graphitic nanostructures characteristic of most examples of catalytic graphitization. The sample prepared from $FeCl_3$ showed much less evidence of graphitic nanostructures in TEM images and appeared to have a high amorphous carbon content. This observation was supported by porosimetry data, which showed

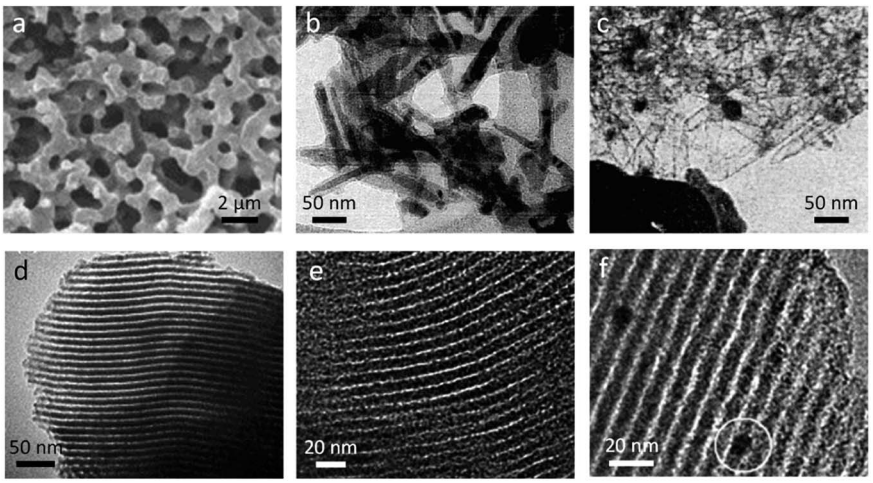

Fig. 7 (a) SEM image of macroporous carbon produced from resorcinol-formaldehyde resin, (b) TEM image of iron hydroxide needles with amorphous carbon coating and (c) the same sample after further pyrolysis, showing empty needle-shaped carbon shells. Also shown are TEM images of (d) Fe-doped SBA-15 mesoporous silica and (e) carbon templated from that silica and f) ordered mesoporous carbon from Pluronic F127-templating of resorcinol formaldehyde with iron nanoparticle circled. Figures modified with permissions from ref. 119, 120, 122 and 124.

mesoporosity in both the iron nitrate and ammonium iron citrate systems but only microporosity in the $FeCl_3$ system (Fig. 8a, d, g). Investigation of the structure of the materials and the mechanism of formation offered insight into the reason for this disparity. Temperature-dependent X-ray diffraction data (Fig. 8b, e and h) showed that all samples initially formed iron oxide (Fe_3O_4) but for iron nitrate and ammonium iron citrate the peaks are very broad indicating nanoparticles. In contrast, the Fe_3O_4 peaks for the sample prepared from $FeCl_3$ were sharp, indicating large crystallites. In the nitrate and ammonium iron citrate systems, the magnetite nanoparticles are reduced to wüstite (FeO) nanoparticles (again indicated by very broad diffraction peaks) before reduction to Fe/Fe_3C. In contrast, the sharp magnetite peaks in the $FeCl_3$ system are transformed to sharp wüstite peaks before reduction to Fe/Fe_3C. SEM images support these observations, with carbons prepared from iron nitrate and ammonium iron citrate containing small nanoparticles of iron, indicated by the bright spots on the back-scattered electron images (Fig. 8c, f, i). The carbon derived from $FeCl_3$, however, shows very large iron particles, which appear to be located mainly on the carbon surface. The authors demonstrate that the reason for the very large particles is the volatility of the $FeCl_3$ precursor driving evaporation of $FeCl_3$ from the loaded microcrystalline cellulose spheres and deposition of large particles on the surface. The work provides further evidence that graphitization is closely linked to catalyst particle size. Interestingly, the iron chloride also influences the carbonization process and particularly the formation of micropores because of its Lewis acid character, which 'activates' the carbon by promoting dehydration rather than depolymerization reactions.[137,138]

Another study compared the graphitization of cellulose, starch and glucose, using iron nitrate as the iron precursor.[108] Cellulose and starch are both composed of polymers that are based on glucose monomers but while glucose is fully water-soluble, cellulose is insoluble and starch only swells to form gels. Pyrolysis of each of these precursors with aqueous iron nitrate resulted in carbons with very different structures, where cellulose and glucose carbons were mesoporous and the starch carbon was primarily microporous and with a much broader graphite XRD peak. Further study of the system showed that a mesoporous graphitic carbon could be formed from starch, but only by extending the pyrolysis time (Fig. 9). Small-angle X-ray scattering data indicated that the iron carbide particles in the starch system grow very slowly, as can be inferred by the broad peaks in X-ray diffraction data. The authors postulated that the complex gel-structure of starch granules allows intercalation of the Fe^{3+} precursor within the constituent amylose and amylopectin molecules (Fig. 10). The thermal stability of starch means that the organic network persists for a long time around the iron precursor as it gradually agglomerates to form iron oxide nanoparticles. Smaller iron oxide nanoparticles would in turn lead to small iron carbide nanoparticles. Glucose, being a small molecule, decomposes much earlier, which would facilitate mass transport of iron species through the developing carbon. In the insoluble cellulose system, the iron is dispersed over the surface, again facilitating mass transport and particle growth. The implication from this data is that there is a critical size of Fe_3C particle that must be reached before graphitization can occur. This is something that has also been suggested by other authors.[116,118]

The other major component of many plant-based biomass sources is lignin. Lignin is an abundant polyaromatic molecule and a waste product of the Kraft wood pulping process, making it a popular candidate for graphitization. The challenge of working with lignin is that it is insoluble in water. To address this, several authors report graphitization of lignin by first dissolving lignin in tetrahydrofuran (THF) and then adding aqueous iron nitrate to maximise homogeneity between the lignin and iron.[139,140] After drying the mixtures and subjecting

Table 3 List of graphitic nanostructures produced from biopolymer precursors

Product description	Organic precursor	Iron source	Temp. (°C)	Comments
Turbostratic carbon with a ribbon morphology[146]	Microcrystalline cellulose spheres	$Fe(NO_3)_3$	800	Detailed mechanism study
Graphitic carbon shells and tube-like structures[147]	Cellulose filter paper	$Fe(NO_3)_3$	800	*In situ* TEM images of graphitization
Iron or iron carbide nanoparticles embedded in graphitic carbon matrix[148]	Cellulose	Iron oxide nanoparticles	Up to 800	Initial hydrothermal treatment
Mesoporous graphitic carbon[149]	Microcrystalline cellulose spheres	$Fe(NO_3)_3$	800	Various metals compared
Carbon encapsulated iron carbide nanoparticles[150]	Cellulose	Fe_3O_4 nanoparticles from $FeCl_2/FeCl_3$	800–1600	Thicker graphitic shell at higher temperature
Mesoporous graphite-containing carbon composites[151]	Cellulose	$FeCl_3/Fe(NO_3)_3$	500–1000	Various cellulose precursors
Mesoporous graphitic carbon[108]	Cellulose fibres	$Fe(NO_3)_3$	800	Compared to glucose and starch, BET surface area 358 $m^2\ g^{-1}$
Porous graphitic carbon[152]	Cellulose	$Fe(NO_3)_3$	850	Liquid, gaseous and solid products characterized
Microporous or mesoporous carbon[108]	Potato starch	$Fe(NO_3)_3$	800	Graphitization very slow compared to cellulose or glucose
Graphitic carbon nanostructures[100]	Starch	$Fe(NO_3)_3$	900	Comparison of starch, glucose and sucrose
Graphitic-carbon-encapsulated iron nanoparticles[141]	Kraft lignin	$Fe(NO_3)_3$	700–1000	Larger particles believed to create thicker graphitic shells
Graphene-encapsulate iron particles, multilayer graphene sheets/flakes, core–shell structure[139]	Kraft lignin	$Fe(NO_3)_3$	1000	Lignin dissolved in THF
Graphene-encapsulated iron particles[140]	Kraft lignin	$Fe(NO_3)_3$	1000	Different iron:lignin ratios
Graphene-encapsulated iron nanoparticles[153]	Kraft lignin	$Fe(NO_3)_3$	1000	Effect of pyrolysis gases investigated: Ar, CO_2, H_2, CH_4
Carbon-encapsulated iron nanoparticles and carbon tubules[154]	Kraft lignin	Fe nanoparticles or $Fe(NO_3)_3$	1000	Comparison of solid and aqueous iron precursors
Core shell structures[155]	Lignin, cellulose and hemicellulose	$Fe(NO_3)_3$	1000	Biomass pyrolyzed before Fe addition and second pyrolysis step. Limited graphitization for lignin
Porous carbon sheets[143]	Agar	$Fe(NO_3)_3$	800	$Al(NO_3)_3$ as templating agent
Graphitic mesoporous capsules, graphitized carbon[156]	Gelatin	$Fe(NO_3)_3$	800	$Mg(NO_3)_3$ to prevent sintering
Sponge-like graphitic carbon[142]	Chitosan	$FeCl_3$, $FeCl_2$ or $(Fe(Phen)_3Cl_2)$	900	Freeze drying of chitosan gel introduces macroporosity
N-doped carbon with a high degree of graphitization[157]	Chitosan	$FeCl_3$	800–1000	Graphitic N functionality

them to pyrolysis under argon, shell-like encapsulated metal nanoparticles were found in the carbon products.[140] Similar shell-like nanostructures were reported by Zhang *et al.*, but rather than solubilizing the lignin in THF, the authors added aqueous iron nitrate to lignin powder.[141] This resulted in a large polydispersity in the catalyst particles, reflecting the fact that the iron would just coat the lignin particles rather than be dispersed throughout the lignin molecules. Interestingly, the authors found some evidence that the number of graphene layers around a catalyst particle may be correlated to the diameter of that particle.

There are many other biopolymers produced by both plants and animals and several of these have been employed in the production of carbons by iron-catalyzed graphitization. Most of

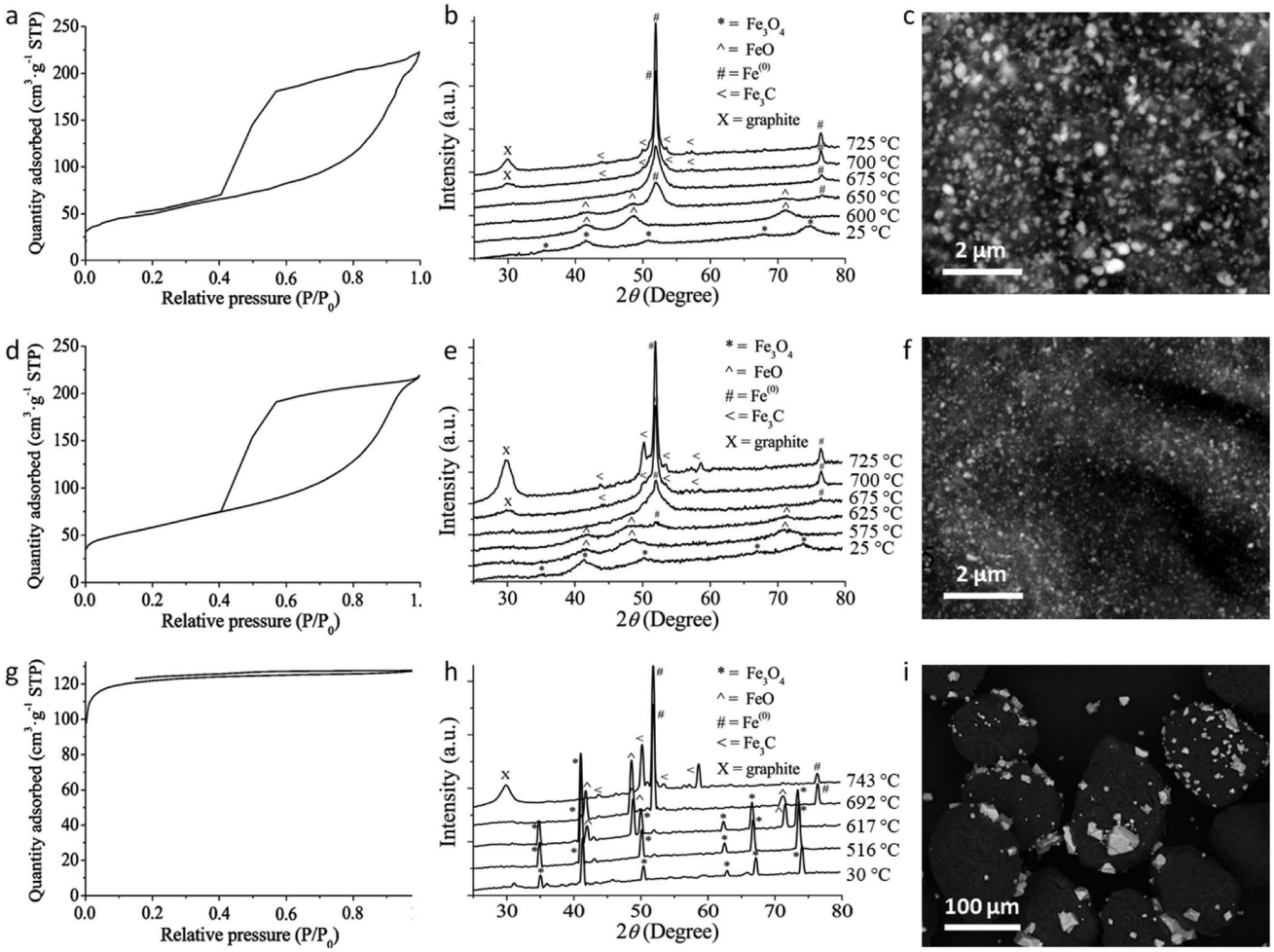

Fig. 8 Nitrogen adsorption/desorption isotherms, temperature dependent X-ray diffraction and SEM (backscattered electron) images of carbons produced from microcrystalline cellulose and (a–c) iron nitrate, (d–f) ammonium iron citrate and (g–i) iron(III) chloride. NB: temperature-dependent XRD was performed on samples preheated to 500 °C. Figures modified with permission from ref. 65.

these examples involve polymers that are soluble in hot water, producing gels that can trap aqueous iron precursors. The gels can then be dried in an oven to produce a dense material or freeze dried to give a sponge-like structure which is retained during pyrolysis.[142] An advantage of many biopolymers is that they contain functional groups which can facilitate dispersion of an ionic iron precursor. For example, agar is derived from seaweed and consists of two polysaccharides (agarose and agaropectin) which contain hydroxyl groups that can coordinate to aqueous Fe^{3+} to produce a precursor for catalytic

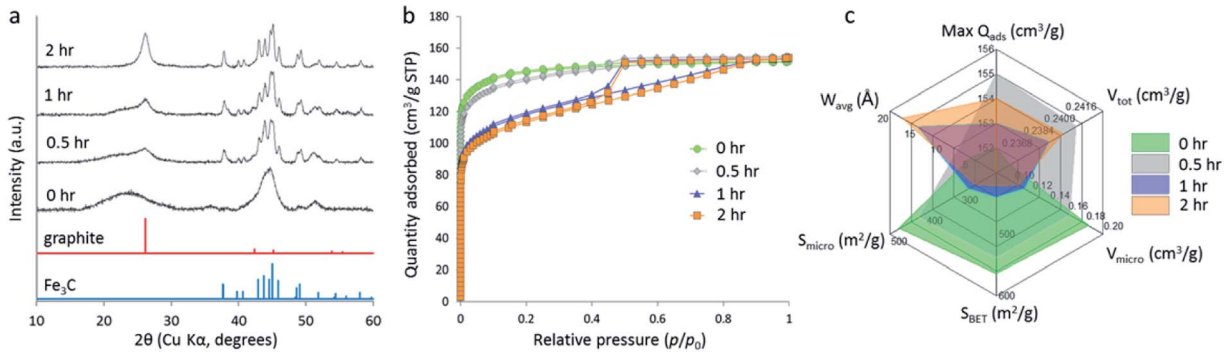

Fig. 9 (a) XRD data, (b) N_2 adsorption/desorption isotherms and (c) porosimetry data for carbons prepared by pyrolyzing starch and $Fe(NO_3)_3$ to 800 °C for various hold-times. Figure reproduced with permission from ref. 108.

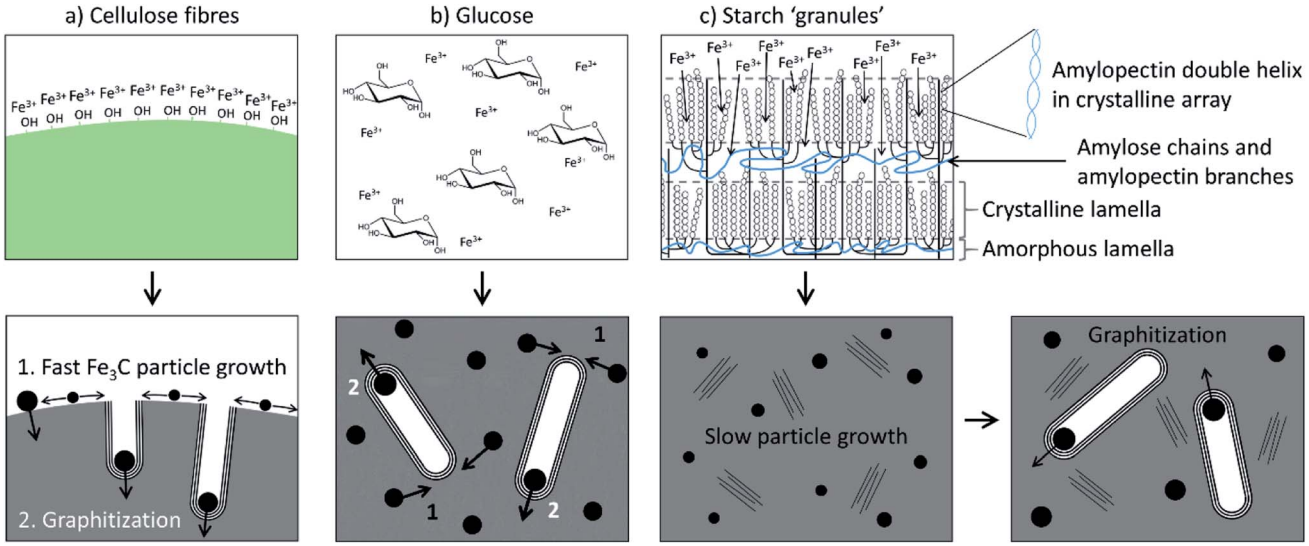

Fig. 10 Schematic of proposed iron-catalyzed graphitization mechanisms for (a) cellulose, (b) glucose and (c) starch. Figure reproduced with permission from ref. 108.

graphitization.[143] Chitosan is another polysaccharide that been used to generate porous graphitic carbons. The advantage of chitosan is that each saccharide monomer contains an amine group, which can facilitate doping of nitrogen into carbons during pyrolysis.[142] A final example is gelatin, which is a polypeptide derived from collagen. Gelatin forms sticky liquids and resins when combined with metal nitrates and these expand to form foams on drying.[144] Like the freeze-dried chitosan sponge, the foam-like structure of the gelatin–metal nitrate mixtures is also maintained during pyrolysis and if gelatin is combined with iron nitrate, the resulting carbon foam contains iron carbide nanoparticles coated in 'onion-like' layers of graphitic carbon.[145]

4.4 Raw biomass

There is considerable interest in the conversion of raw biomass into functional carbon materials for various applications and there are some excellent reviews of this specific field.[20,158] For catalytic graphitization using iron-precursors, one of the most interesting features of products derived from biomass is that they maintain their macrostructure during pyrolysis (Fig. 11a). This is not just aesthetically attractive. Biological materials encompass a wide range of complex and highly evolved structures and capturing these in a functional material can give unique properties.[159] For example, the interconnected pore structure of wood is maintained during iron-catalyzed graphitization, leading to advantageous properties for the resulting carbon in supercapacitors.[54] While normal (iron-free) pyrolysis will also maintain the macrostructure of biomass, the addition of iron catalysts introduces mesoporosity through the formation of graphitic nanostructures. Doping biomass with iron salts leads to the formation of Fe or Fe_3C nanoparticles during pyrolysis. These nanoparticle catalysts drive graphitization, as in examples earlier in this review. However, in raw biomass, the catalyst nanoparticles often appear to be highly mobile, driving conversion of the biomass-derived amorphous carbon into a dense network of graphitic carbon nanotubes (Fig. 11b–d).[160] The fact that the Fe or Fe_3C nanoparticles produce the graphitic nanostructures means that the size of the catalyst particles directly impacts the porosity of the resulting carbon. This can be observed in nitrogen porosimetry data of graphitic carbons produced from $Fe(NO_3)_3$/sawdust at various ratios (Fig. 11e), where a higher Fe-content leads to larger pores. This can also be observed in TEM images, (Fig. 11f/g) which show much smaller particles at a lower Fe/sawdust ratio. Interestingly, the degree of graphitization does not seem to be affected by a significant drop in iron content, possibly indicating that the smaller Fe/Fe_3C catalyst particles travel further through the amorphous carbon matrix. The broad graphitic peak in X-ray diffraction patterns of these samples suggests that the graphitic carbon nanotubes have a high level of disorder, resembling a turbostratic rather than a truly graphitic carbon. In a similar system, Gomez-Martin *et al.* showed that pyrolysis of $FeCl_3$-doped wood samples to higher temperatures (1000–2000 °C) leads to a much sharper graphitic peak, indicating more regular graphitic structure.[51] There is a drop in the BET surface area at higher temperatures (200 $m^2 g^{-1}$ at 850 °C to 31 $m^2 g^{-1}$ at 2000 °C) but this is still higher than a control sample (no Fe) pyrolyzed to 2000 °C, showing that some of the porosity can be maintained. This is reflected in TEM images, which still identify graphitic nanostructures in $FeCl_3$-doped wood pyrolyzed to 2000 °C.

A factor that must be considered in iron-catalyzed graphitization of biomass is the ability of the iron salt to penetrate the biomass structure. Many authors mill biomass to a fine powder before infiltration with an iron salt to maximize coating of the biological material in iron. Hunter *et al.* demonstrated this systematically, showing that milling a wide range of biomass precursors before iron-catalyzed graphitization led to porous graphitic carbons with consistent adsorptive properties. Another consideration is the nature of the iron precursor. Liu *et al.*

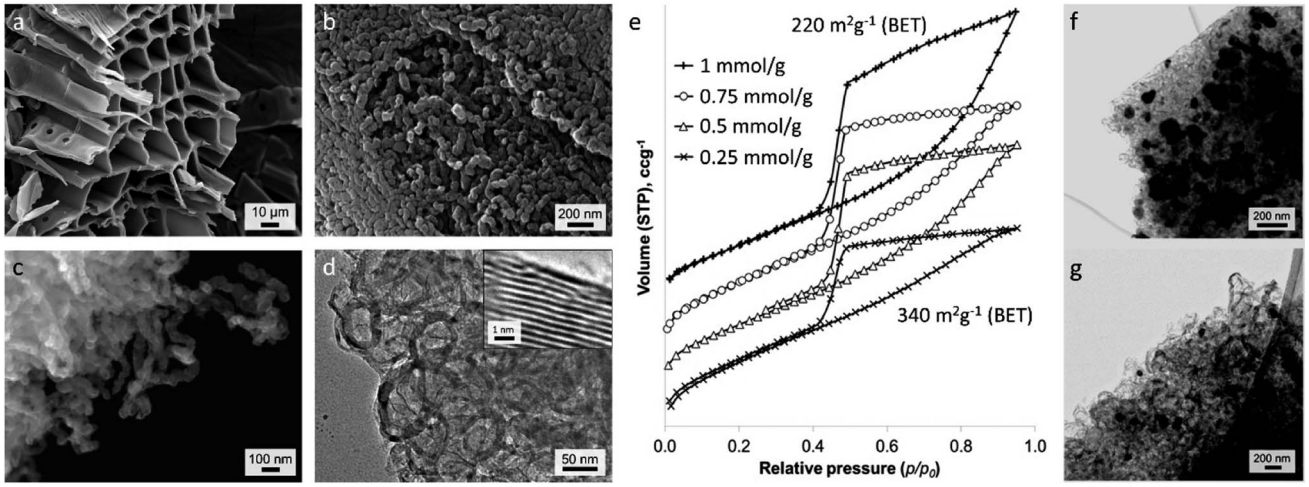

Fig. 11 (a–c) SEM and (d) TEM images of carbon produced from iron-catalyzed graphitization of sawdust. (e) N_2 adsorption–desorption isotherms (offset along *y*-axis) of graphitic carbons produced from $Fe(NO_3)_3$ and sawdust at various Fe/biomass ratios and TEM images of samples prepared from (f) 1 mmol and (g) 0.5 mmol $Fe(NO_3)_3$ per gram of sawdust. Images modified with permission from ref. 160.

describe an intriguing process using $FeCl_3$ as a catalyst for carbon nanotube production from sawdust.[161] Their process involves a fast pyrolysis step, where powdered sawdust is loaded with an iron salt, dried, flushed with N_2 and then inserted into a preheated quartz tubular reactor (Fig. 12a).[162] The resulting carbon powder was covered in a dense mat of graphitic nanotubes (Fig. 12b). The authors demonstrate that the rapid heating leads to degradation of the cellulosic precursor into volatile low molecular weight hydrocarbons. These dissolve into surface Fe or Fe_3C nanoparticles to drive the formation of graphitic nanotubes in a process analogous to chemical vapour deposition. Interestingly, $Fe(NO_3)_3$ and $Fe_2(SO_4)_3$ catalysts did not produce the surface mat of graphitic nanotubes (Fig. 12c) and neither did $CuCl_2$ or $NiCl_2$, indicating that the combined catalytic effect of iron and chloride is required for this phenomenon to occur. Zhang *et al.* reported similar structures from the fast pyrolysis of $FeCl_3$-treated rice husks.[163] It is possible that the unique behaviour of $FeCl_3$ derives from the Lewis acid character of this salt, which is known to change the decomposition pathway of cellulosic materials.[164–166] There are many other examples of raw biomass being used to produce graphitic carbons and it is difficult to draw further conclusions due to the large range of iron precursors and pyrolysis conditions used. For the benefit of the reader, these are summarized in Table 4.

4.5 Organometallics

The examples discussed in the preceding sections have all used a separate organic and metal precursor. An alternative method is to use a single reactant containing both components, *i.e.*, an

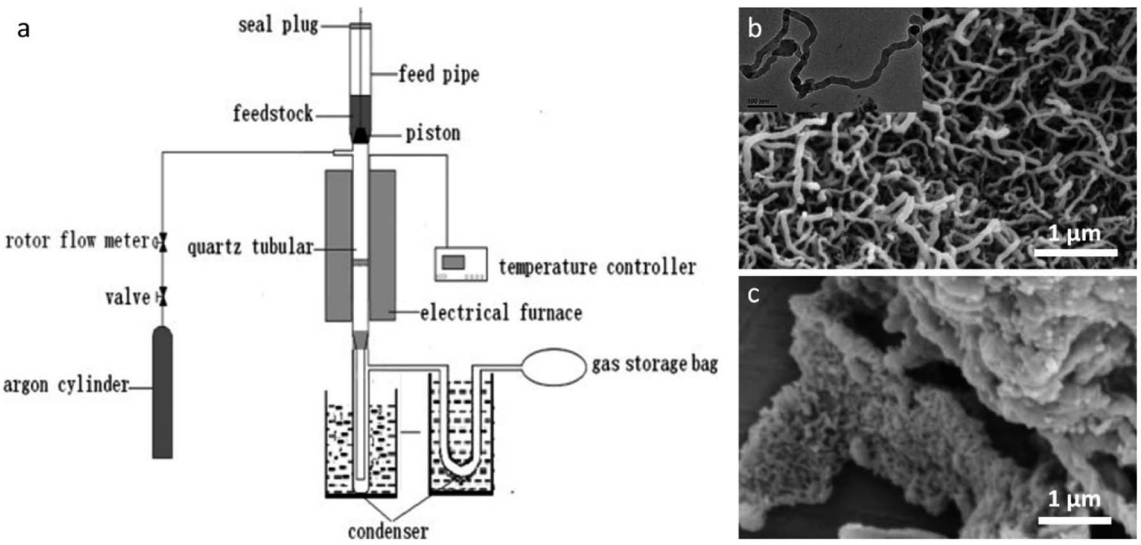

Fig. 12 (a) Diagram of setup for fast pyrolysis and SEM images of samples prepared by fast pyrolysis of sawdust powder with (b) $FeCl_3$ (inset TEM image) and c) $Fe(NO_3)_3$. Figures modified with permission from ref. 161 and 162.

organometallic complex containing iron (Table 5). This route has been less widely explored but there are some examples of direct pyrolysis of iron complexes such as iron gluconate.[191] One challenge with organometallic precursors is their lack of thermal stability or even volatility. Some authors have resolved this by polymerizing the precursor, *e.g.*, the catalytic cross-linking of ferrocene.[192] Another approach is to exploit the volatility of the precursor. For example, Leonhardt *et al.* used one furnace to drive sublimation of ferrocene before passing the vapour into a second furnace at a much higher temperature, where carbon nanostructures were deposited onto a substrate.[193] A similar approach has been used to produce graphitic nanocages by bubbling a mixture of nitrogen and carbon-rich gas such as acetylene through liquid iron pentacarbonyl and passing the resulting vapour through a tube furnace.[194,195] High pressure reactors have also been used for catalytic graphitization of ferrocene.[196] A final note on the use of organometallic prearccursors is that they can be readily templated. Lee *et al.* mixed iron phthalocyanine with mesoporous silica (SBA-15) in a pestle and mortar. Pyrolysis resulted in sublimation and decomposition of the iron phthalocyanine and deposition of graphitic carbon and iron nanoparticles through the silica structure.[197] The silica can subsequently be removed with HF or NaOH and the resulting carbon retains the high porosity and surface area (877 $m^2\ g^{-1}$) of the template.

5. Mechanism of catalytic graphitization

One of the current drawbacks of catalytic graphitization is the limited understanding of the mechanism. As seen in the sections above, there are many examples of graphitic nanostructures synthesized by pyrolysis of organic and iron precursors. The choice of precursors and synthesis conditions vary greatly between different studies and can all significantly affect the chemistry and structure of the graphitic carbon product. As a result, it is difficult to directly compare different systems or predict which may result in graphitic carbon materials with enhanced properties. Future development of the method of catalytic graphitization requires a more detailed understanding of the mechanism. While there are few studies on the mechanism of catalytic graphitization in pyrolysis, there has been considerable effort to understand the process of CVD synthesis of carbon nanotubes.[200,201] The processes are fundamentally different. CVD synthesis of carbon nanotubes involves decomposition of a hydrocarbon gas and dissolution of carbon into a catalyst particle. In contrast, catalytic graphitization involves decomposition of an organic precursor into amorphous carbon and graphitization of that *solid* carbon by a catalyst particle. However, it may be possible to gain insight into the mechanism of catalytic graphitization by studying CVD chemistry.

5.1 Insights from CVD synthesis of carbon nanotubes: nucleation and growth

As noted in section 2.3, CVD synthesis of carbon nanotubes can occur by float growth or base growth. In both situations, the first step is the initial nucleation of solid carbon from the catalyst particle. A popular theory for nucleation of carbon nanotubes on catalyst particles is known as the "yarmulke" mechanism, first proposed by Dai *et al.*[202] The yarmulke mechanism involves the initial formation of a graphene 'cap' over the catalyst nanoparticle, which is stabilized by binding of the edges to the catalyst nanoparticle. Computer simulations have been widely used to probe the precipitation of carbon from saturated Fe_xC_y catalyst nanoparticles and the formation of the graphene cap as the first step to SWCNTs.[203] As new carbon is introduced to the catalyst particle, the cap lifts of the catalyst and elongates to form a SWCNT (Fig. 13a). Successful detachment of the cap and thus nanotube growth is dependent on multiple factors such as temperature and work of adhesion of the graphitic cap on the nanoparticle, which is governed by the interfacial energy and thus linked to chemical and physical properties of the catalyst particle.[204] Cap lift-off and nanotube growth has been observed experimentally using *in situ* environmental TEM (Fig. 13b).[205,206]

Simulations have also shown the possibility of cap formation followed by growth to form a continuous shell around the catalyst particle.[207] This is believed to occur when there is not enough energy to overcome the interfacial energy between the cap and the catalyst and correlates to experimental observations of graphitic shells coating catalyst particles in CVD. Factors that appear to contribute to shell formation include particle size (very small particles are not encapsulated), catalyst phase (Fe or Fe_3C) and temperature (encapsulated particles tend to be found in the lower temperature regions of CVD ovens). Interestingly, there is evidence that the number of 'shells' of graphite around a catalyst particle is linked to the diameter of that particle. Given that the addition of carbons to the edge of an existing graphene sheet is energetically more favourable than nucleation of a new sheet, it is believed that the first shell is completed before a new shell nucleates underneath. This would lead to exhaustion of the carbon supply in the catalyst, which could explain experimental evidence that encapsulated particles in CVD synthesis tend to be formed of Fe rather than Fe_3C.[208] Catalytic graphitization leads to similar 'encapsulated' and tube-like structures, suggesting that there may be parallels with the processes of CVD. However, while some examples of catalytic graphitization produce mainly shells and others mainly tubes, there are also plenty of examples where a mixture of products is formed.

Another feature of catalyst diameter is that it influences the diameter of the resulting carbon nanotube. This is believed to be due to cap lift-off occurring after the cap reaches a similar diameter to the catalyst cluster.[209] Cheung *et al.* demonstrated experimentally that monodisperse iron nanoparticles could be used to produce carbon nanotubes with controlled diameter *via* CVD.[210] These authors also note that an efficient carbon supply is required to drive the growth of large-diameter nanotubes from large catalyst particles. On the other end of the scale, catalyst clusters that are too small (<20 atoms) have been shown in simulations to produce poor quality carbon nanotubes, due to inconsistencies in binding between the cluster and the dangling bonds of the nanotube.[211] This reflects some experimental observations that nanoparticles must reach a critical

Table 4 List of graphitic carbon structures produced by iron-catalyzed graphitization of biomass

Product description	Organic precursor	Iron source	Temp. (°C)	Comments
Continuous and bamboo-like graphitic nanotubes[160]	Softwood sawdust	$Fe(NO_3)_3$	800	Porosity depends on iron:biomass ratio
Nanofibers/mesoporous carbon composites[161]	Sawdust	$FeCl_3$	600–800	Fast pyrolysis process, comparison of $Fe(NO_3)_3$ and $Fe_2(SO_4)_3$
Graphitic carbon nanostructures[167]	Pine wood sawdust	$Fe(NO_3)_3$	900/1000	Comparison to Ni
Onion-like structure, curved graphitic shells[168]	Beech wood	$FeCl_3$	1000/1300	Impregnation with $FeCl_3$ solution in isopropanol
Porous graphitic carbons[54]	Beech wood	$FeCl_3$	1000–1600	Slow pyrolysis to 500 °C to reduce cracking
Onion-like graphitic shells[51]	MDF wood	$FeCl_3$	850–2000	Slow pyrolysis to 500 °C to reduce cracking
Mesoporous graphitic carbons[66]	Bamboo, nut shells, grasses, wood	$Fe(NO_3)_3$	800	Mechanical milling increases graphitization for hard biomass
Carbon microfibres with iron nanoparticles[169]	Bamboo	$Fe(NO_3)_3$	800	Hydrothermal pre-treatment of bamboo in NaOH
Porous graphitic carbon[170]	Bamboo	K_2FeO_4	800	Bamboo pyrolyzed to 400 °C before infiltration with iron precursor
Porous graphene-like nanosheets[171]	Coconut shell	$FeCl_3$	900	$ZnCl_2$ used for simultaneous activation and graphitization, BET surface area 1874 $m^2\ g^{-1}$
Porous graphitic carbon[172]	Coconut shell	$Fe(NO_3)_3$	1000	Coconut shell milled to a powder before infiltration with $Fe(NO_3)_3$
Magnetic nanofibers/porous carbon composites[163]	Rice husk	$FeCl_3$	600	Various pretreatments of rice husk including hydrothermal and NaOH
Fe/N-doped carbon[173]	Soy bean milk	$FeCl_3$	600–1000	BET surface areas 879–1164 $m^2\ g^{-1}$
Onion-like graphitic carbon[174]	Cotton	Iron(III) acac	650	DMF solvent
Nanoporous carbon@carbon fibre composites[175]	Cotton	$FeCl_3$	500–600	MOF precursor, initial activation step
Mesoporous carbon/iron carbide nanocomposite[176]	Cotton fabric	$Fe(NO_3)_3$	800	BET surface area 154–410 $m^2\ g^{-1}$
Nitrogen-doped porous graphitic carbon[177]	Water hyacinth	$Fe(NO_3)_3$	700	Dopamine hydrochloride as N source
Hierarchically porous carbon nanosheets[178]	*Moringa Oleifera* stems	$FeCl_3$	800	$ZnCl_2$ as activation catalyst
Graphitic core–shell structures[179]	Miscanthus grass powder	$Fe(NO_3)_3$	900	Graphitization enhanced with cobalt
Magnetic carbon nanocages[180]	Pine tree resin	$Fe(NO_3)_3$	1000	Fe_3C catalyst
Hierarchical porous graphitic carbon[181]	Chopsticks	$Fe(NO_3)_3$	850	Potassium oxalate as activating agent
Worm-like structures, carbon nano-capsule[182]	Chinese chestnuts	$Fe(NO_3)_3$	400–800	Gas and liquid byproducts also characterized
Graphitized carbon nanosheets[183]	Citrus grandis skins	$FeCl_3$	1200	Biomass milled, $ZnCl_2$ cocatalyst
Carbon-shell coated iron nanoparticles[184]	Coffee grounds	$Fe(NO_3)_3$	800	Coffee grounds washed before infiltration with $Fe(NO_3)_3$
Mesoporous graphitic carbon[185]	Chestnut shell, bamboo, poplar, cotton, lotus	$Fe(NO_3)_3$	800	Different iron loading and pyrolysis conditions investigated
'Graphite-shell-chains'[186]	Wood, coffee, tofu residue, cotton	$Fe(NO_3)_3$	850	Electron microscopy shows tube-like structures
Graphitic structures[187]	Oil palm frond	$Fe(NO_3)_3$	1000–1400	Silica also added

Table 4 (*Contd.*)

Product description	Organic precursor	Iron source	Temp. (°C)	Comments
Graphitized porous carbon[188]	Phoenix tree leaves	K_2FeO_4	650–950	Pyrolyzed biomass (400 °C) mixed with K_2FeO_4 powder
Carbon shells/tubes[189]	*Oryza sativa* pulp	$FeCl_3$	800	NaOH pretreatment
Porous graphitic carbon microtubes[190]	Willow catkins	$K_4Fe(CN)_6$	900	$FeCl_2$ comparison

size before they become catalytically active in CVD.[212] A similar level of control of nanotube diameter has also been seen in catalytic graphitization. If catalyst particles are smaller, they produce nanotubes and shells of smaller diameter, which is reflected in the porosity of the carbon material.[65,160] A point to note is that many authors have observed Fe or Fe_3C nanoparticles to be 'liquid-like' during the graphitization process and very quickly agglomerate to form larger particles. Controlling this process may be a route to a wider range of graphitic products.

5.2 Insights from CVD synthesis of carbon nanotubes: types of growth

Nanotube growth in CVD can proceed in two different ways depending on specific reaction conditions. One possibility is tip-growth, otherwise known as float-growth, in which the catalyst nanoparticle detaches from the substrate and leaves a carbon nanotube trail between itself and the substrate (Fig. 4).[213] Alternatively, nanotube formation can proceed *via* base-growth, in which the catalyst nanoparticle remains in contact with the substrate and the nanotube grows outwards from the nanoparticle.[214] The dominating mechanism is dependent on the interactions between the catalyst nanoparticle and the substrate, demonstrated by the work of Wang *et al.* in which iron was used as a catalyst and the nature of the substrate was varied.[215] They suggested that if the interfacial energy between the catalyst particle and the substrate is greater than the surface energy of the substrate itself, tip-growth would dominate, which they observed with a silica substrate. Conversely, with a tantalum substrate, the iron/tantalum interfacial energy is lower than the surface energy of pure tantalum so base growth was the dominant pathway. While non-carbon interfaces are generally not relevant to iron-catalyzed graphitization, it will still be important to consider the different interfacial energies that may contribute to catalyst movement.

A second important observation from CVD nanotube growth is that of continuous and bamboo-like carbon nanotubes. As the name suggests, bamboo-like carbon nanotubes resemble the structure of bamboo, with regular compartment-like graphitic structures (Fig. 14a).[216] This contrasts with the straight channel formed in normal carbon nanotubes (Fig. 14b/c). Bamboo-like carbon nanotubes are believed to form by periodic nucleation steps, where a series of graphitic layers form across the trailing edge of the catalyst particle during float growth (Fig. 14d). The catalyst particle then detaches from the graphitic layers and moves forward before stopping to generate another nucleation point.[217] Simulations suggest that bamboo-like carbon

Table 5 List of graphitic nanostructures synthesized from organometallic precursors

Product description	Precursor	Temp. (°C)	Comments
Mesoporous graphitic carbon[197]	Iron phthalocyanine	900	Mesoporous silica template, BET surface area 877 $m^2\ g^{-1}$
Multi-walled carbon nanotubes[198]	Iron phthalocyanine	850	Initial vaporization at 650 °C, then flow of gas into second high T furnace with Ar
Graphitic carbon nanostructures, nanocapsule/nanopipes[191]	Iron(II) gluconate	900–1000	$KMnO_3$ post-treatment to remove iron species and amorphous carbon
Graphitic porous carbons with 3D nanonetwork[192]	Ferrocene	700–900	Initial reflux in $CCl_4/AlCl_3$ to drive crosslinking of cyclopentadienyl rings
Fe-filled carbon nanotubes[193]	Ferrocene	860–920	Initial sublimation of ferrocene at 150 °C, then flow of gas into second high T furnace with Ar
Graphitic nanocages	$Fe(CO)_5$, acetylene and ammonia	750–1050	Nitrogen doping in product
Graphitic nanocages	$Fe(CO)_5$ and ethanol	900	Vertical tube furnace with three heating zones
Carbon-encapsulated iron carbide nanoparticles[196]	Ferrocene	600–1600	High pressure, mechanism study
Core@shell nanocomposites[199]	Ferrocene	900	High pressure

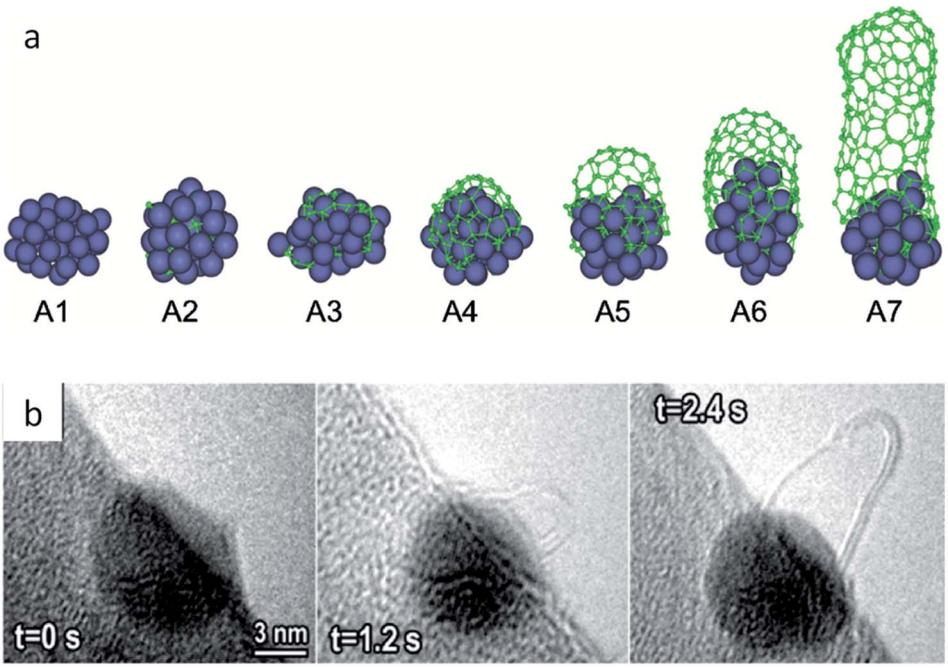

Fig. 13 (a) Molecular dynamics simulation of carbon cap formation and lift-off and (b) still images taken from environmental TEM video footage of carbon nanotube growth from an iron catalyst. Images modified with permission from ref. 204 and 205.

nanotubes form in conditions of higher carbon concentration,[218] which correlates to an *in situ* TEM study which identified Fe_3C as the catalyst for bamboo-like carbon nanotubes and Fe as active for continuous carbon nanotubes.[216]

Continuous and 'bamboo-like' nanotubes have also been identified in many reports of catalytic graphitization, sometimes within the same sample.[160] Given that many reports of catalytic graphitization identify both Fe_3C and Fe in X-ray diffraction data, it is possible that the different materials drive two different types of graphitization. Some interesting insight comes from work by Ichihashi *et al.*, who grew amorphous carbon 'nanopillars' by electron-beam-induced chemical vapor deposition on an iron-doped carbon substrate.[219] On heating the sample to 650 °C inside a transmission electron microscope, they observed the formation of iron nanoparticles in the substrate followed by 'liquid-like' movement of particles outwards along the carbon pillars, leaving a graphitic 'trail' behind (Fig. 15). In one case, they observed the liquid-like particle moving at constant speed along the carbon nanopillar to form a multi-walled nanotube. In another case, the catalyst

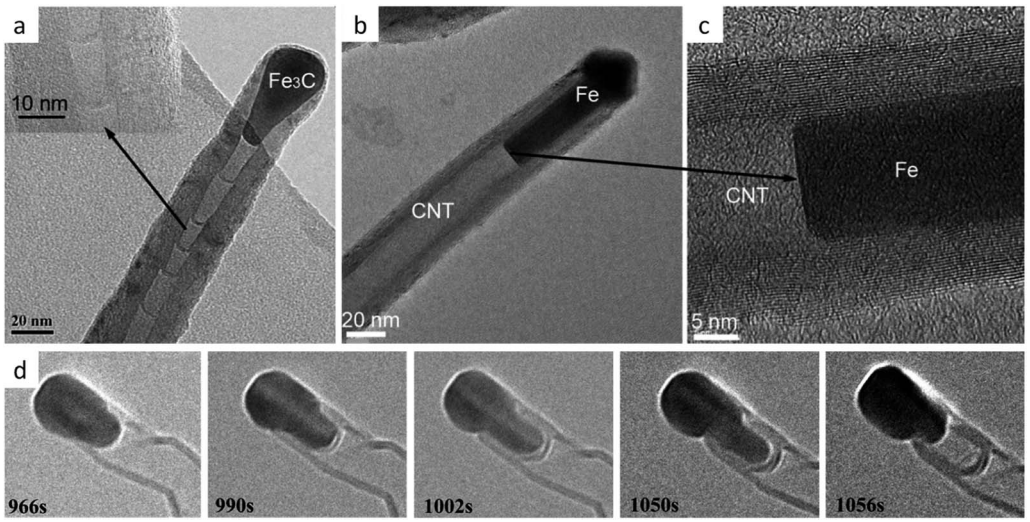

Fig. 14 TEM images of (a) bamboo-like and (b and c) continuous carbon nanotubes and (d) *in situ* growth of a bamboo-like carbon nanotube. Figures modified with permission from ref. 216 and 217.

particle moved more slowly, and the tail of the particle periodically paused for several hundred milliseconds, forming graphene caps within the nanotube. Crucially, the nanoparticle catalysts never moved back along the pillar once graphitization was complete, indicating that graphitic carbon does not redissolve in the catalyst once it has formed. The authors do not propose a reason for the different behaviour, but they do suggest that the driving force for movement is due to the difference in solubility of amorphous carbon in iron compared to graphitic carbon in iron. A difference in solubility of amorphous carbon in Fe compared to Fe_3C could potentially then be a reason for slower or faster movement of a catalyst particle through amorphous carbon.

5.3 The chemical nature of the catalyst

In CVD synthesis and in catalytic graphitization, the chemical nature of the catalyst is a matter of debate. The high activity of iron-based catalyst particles is commonly credited to the high solubility of carbon in iron at temperatures of around 700–800 °C. One of the proposed mechanisms by which graphitization occurs is dissolution-precipitation. Here, the iron particle dissolves carbon atoms until it reaches a point of supersaturation, at which point graphitic carbon is precipitated from the particle. This hypothesis has been used to explain why transition metals with a low carbon solubility such as copper show poor catalytic activity for graphitization, while metals with high carbon solubility such as iron and nickel show high activity.[139] An alternative theory suggests that the formation of metastable carbides is crucial to graphitization. These decompose into a more thermodynamically stable metal species and precipitate graphitic carbon in the process. There is evidence for Fe[220] and Fe_3C[221] being the active catalyst for CVD synthesis of carbon nanotubes and other authors have shown that both phases can be active catalysts, but for different graphitic products.[216] Fe and Fe_3C are both phases that are commonly identified in *in situ* X-ray diffraction studies of iron-catalyzed graphitization, often within the same sample.[146,149,222,223] This raises the possibility that both dissolution-precipitation and carbide decomposition are potential mechanisms in catalytic graphitization. However, other pathways may also be possible. For example, a study by Yan *et al.* proposed that as iron carbide is stable at the temperatures involved in catalytic graphitization, it is unlikely that the formation of graphitic carbon is due to metal carbide decomposition. Instead, they suggested that the iron carbide and pure iron species may both act as dissolution-precipitation catalysts, contributing to a high catalytic activity in iron species.[139]

An important point to note is that the crystal phases present during catalytic graphitization may change as the sample is cooled. For example, *in situ* synchrotron XRD data from Gomez-Martin *et al.* showed that the onset of graphitization of a wood precursor corresponded to the appearance of an Fe_3C phase.[222] During cooling, the Fe_3C phase transforms to γ-Fe then α-Fe, triggering a second carbon precipitation step. This change in the crystalline composition on cooling highlights the importance of studying graphitization *in situ*. Systems that are only studied after removal from the furnace will offer limited information on the mechanism by which they were formed.

Another question that is linked to the chemical nature of the catalyst is how carbon is transported within the catalyst particles. Again, much of the evidence so far on this phenomenon comes from studies of CVD processes. For example, Yoshida *et al.* collected *in situ* environmental TEM footage of MWCNTs growing from Fe_3C nanoparticles.[221] All the cylinder layers of the nanotube were observed to grow at the same rate, regardless of diameter, which strongly suggests migration of carbon atoms through the bulk of the catalyst particle. Other examples propose diffusion of carbon atoms around the surface of the catalyst nanoparticles. Again, there is a possibility that different mechanisms operate in different systems. In the complex world of iron-catalyzed graphitization, there may even be multiple mechanisms operating within the same sample.

The mechanism of iron-catalyzed graphitization can be further complicated when considering doping, or the presence of impurities within the system. Doping of Fe–C materials with heteroatoms has been an intense field of study as it has led to improved performance in various applications. For example, N-doped carbons that contain iron species are known to be highly active in the oxygen reduction reaction[224,225] and N-doped carbons are also of interest in lithium-ion batteries.[226] There is also considerable interest in phosphorus[227] and sulfur[228]-doped carbons. Given that iron can form alloys with nitrogen, phosphorus and sulfur, it is reasonable to assume that the presence of these heteroatoms will influence the chemistry of Fe–C graphitization catalysts, whether or not the heteroatoms become integrated into the resulting graphitic carbon. While there are few studies on the effect of heteroatom doping on

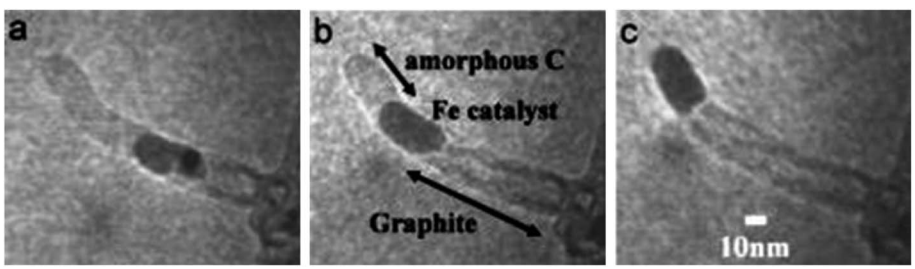

Fig. 15 Images from an environmental TEM video showing movement of an iron catalyst particle along a carbon 'nanopillar'. Figure modified with permission from ref. 219.

graphitization catalysts, it is clear that the presence of these species affects graphitization. For example, sulfur doping was shown to affect the number of layers in carbon nanotubes grown by CVD.[229] Sulfur has also been used to prevent agglomeration of iron catalyst particles during CVD, which in turn controls the diameter of the carbon nanotubes.[230] It is possible that iron sulfide (FeS) or iron nitride (Fe_3N) may act as graphitization catalysts in their own right. For example, there have been reports of graphitic structures forming around iron sulfide nanoparticles.[231] A final point that is worth noting is that different nitrogen-containing precursors can lead to different types of nitrogen feature in the resulting graphitic carbon, which suggests that the precursor can affect the mechanism of graphitization.[232]

5.4 The physical nature of the catalyst

Determining the physical state of the catalyst particle during graphitization is also challenging. A commonly cited theory describing the physical state of the catalyst in CVD processes is the vapour-liquid-solid mechanism first proposed by Wagner and Ellis to explain the growth of silicon whiskers.[233] This mechanism suggests that the catalyst particle must be in a liquid state to promote growth. However, the melting temperature of bulk iron is 1538 °C,[234] much higher than typical reaction temperatures in CVD and catalytic graphitization. Despite this, many *in situ* environmental TEM studies have observed 'liquid like' behaviour.[235] Harutyunyan *et al.* proposed that the formation of a liquid phase is essential for growth of carbon nanotubes in CVD and the formation of a solid particle hinders growth.[236] Other authors, however, show evidence that the catalyst particle remains in the solid state (demonstrated by the presence of lattice fringes in *in situ* TEM images) and that the 'liquid-like' behaviour is due to the constant fluctuation of the catalyst nanoparticle phase.[221] While many of the environmental TEM studies have probed CVD processes, similar liquid-like behaviour has been observed in the iron-catalyzed graphitization of cellulose (Fig. 16). The catalyst particle was observed to move through the solid carbon matrix with the front edge of the particle creeping slowly forwards and dissolving the amorphous matrix. The trailing edge of the particle moves in a very different way and stops periodically to allow build-up of graphitic layers before suddenly detaching and moving forward very quickly. This implies that the interfacial tension between the catalyst and the graphene surface is very different to the interfacial tension between the catalyst and the amorphous carbon.[147] The video footage showed that the particle stopped moving once the amorphous carbon was exhausted. Interestingly, the experiment also showed that some particles remained stationary throughout the experiment, which may indicate that some particles became encapsulated in graphite or that they were composed of an inactive phase.

Computer simulations have been used to offer insight into the physical properties of the graphitization catalyst. Methods such as molecular dynamics have shown that the melting temperature of metal nanoparticles can be considerably lower than the corresponding bulk material, raising the possibility that graphitization catalysts may be in a liquid or liquid-like state.[237] One model, carried out by Ding *et al.*, suggests that both states are possible.[238] Their study modelled the growth of single-walled carbon nanotubes on both solid and liquid iron particles and found that the two routes had similar growth mechanisms. The main difference was that the main diffusion pathway of the carbon atoms in liquid nanoparticles was through the bulk, while surface diffusion dominated in solid nanoparticles. In real systems, it may be that both routes take place at the same time, because catalyst particles are unlikely to be completely uniform in size. It is possible that the smaller particles are in a liquid state and the larger particles in a solid state at the same temperature. The study by Ding *et al.* not only suggests that this is plausible, but that the resulting nanostructure may be the same in both scenarios. A further factor to consider is that some metals, including iron, are known to undergo surface melting. This may provide an explanation for the liquid-like behaviour of the catalyst particles in some systems. Ding *et al.* have used molecular dynamics to demonstrate that surface melting occurs at temperatures below the melting temperature in both free[239] and supported iron nanoclusters,[240] with the depth of the surface melt increasing with temperature until the cluster undergoes complete melting. Therefore, as well as both solid and liquid states, it is possible that the nanoparticles occupy 'in-between' states in the process of graphitization. Modelling can never take into consideration all the factors of an experimental study. One important consideration when considering the size effect is the introduction of a surface, which is applicable to both CVD and catalytic graphitization processes. While stronger interactions caused by a lower contact angle can decrease the melting temperature,[241] favourable epitaxy between the nanoparticle and the substrate can raise the melting temperature by hundreds of degrees.[242] This implies that the suggested variation in melting temperature may not be a purely size-based argument. There are many more challenges and discoveries remaining in this field.

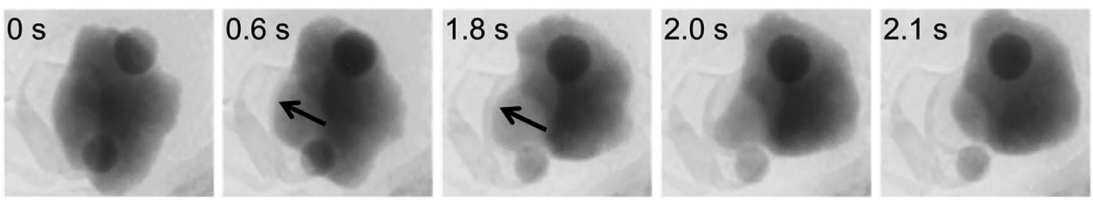

Fig. 16 Still images from *in situ* ETEM footage of an iron-rich particle moving through a carbon matrix. Arrows show the layers of graphite forming on the trailing edge of the catalyst. Images modified with permission from ref. 147.

5.5 *In situ* methods for studying the mechanism of graphitization

The need to understand the mechanism of catalytic graphitization has required the development of novel *in situ* methods. By following the graphitization reaction as a function of time and temperature, it is possible to determine the extent of graphitization and the presence of phase transformations or reactions between carbon and the catalyst. Two *in situ* methods, X-ray diffraction and transmission electron microscopy, have received the most attention. In the case of X-ray diffraction, one of the earliest accounts is from Fitzer and Weisenburger, who devised a special heating stage to follow graphitization of coke (without any catalyst) using a laboratory diffractometer.[243] More recent papers from Hoekstra *et al.* studied the *in situ* pyrolysis and graphitization of microcrystalline cellulose spheres with copper, nickel, cobalt and iron.[65,146,149] These studies used a commercially available heating stage on a laboratory X-ray diffractometer to identify the crystalline phases present during pyrolysis and confirmed the presence of iron oxide intermediates and both Fe_3C and Fe during the graphitization step. The availability of synchrotron sources has enabled experiments with better time resolution. These experiments are technically challenging, due to the need to hold the samples in a quartz capillary in the synchrotron beam, while heating and maintaining an inert atmosphere. Some studies used nitrogen gas flow through[223] or around[244] the capillary while another partially carbonized the sample before sealing it within a quartz capillary.[222] In all these studies, a hot air blower was used to heat the sample to the required temperature (Fig. 17). Despite the very different set-up to a laboratory furnace, the capillaries appear to replicate the conditions of a laboratory furnace effectively.[245] There are many other synchrotron techniques that have been used to study carbon materials or graphitization by other metals. For example, synchrotron based XPS was employed to study the growth of carbon nanotubes using ZrO_2 nanoparticles as catalysts in a low-pressure CVD system. While Zr metal can catalyze graphitization at very high temperatures,[246] Steiner *et al.* found that the catalytic effect for nanotube growth of ZrO_2 took place without carbothermal reduction, with no visible changes in the Zr 3d XPS spectrum during synthesis.[247] Other authors have used *in situ* synchrotron small-angle X-ray scattering (SAXS) to probe the (catalyst-free) pore structure of polyacrylonitride-based carbon fibres during graphitization.[248] Undoubtedly, similar methods will be applied to the question of iron-catalyzed graphitization in the future.

In situ or environmental TEM has also been used to study graphitization of carbon by iron and other metals. The challenge in these experiments again is replicating the laboratory furnace environment as closely as possible. Since electron microscopes operate under a high vacuum, it is necessary to be cautious when interpreting results from *in situ* TEM experiments as the materials may behave differently in the vacuum compared to the N_2 or Ar atmosphere of the laboratory furnace. It is also important to consider how the high energy electron beam may be interacting with the sample. The earliest example of *in situ* TEM investigations of graphitization come from Krivoruchko *et al.*[235] The authors dispersed iron hydroxide particles over an amorphous carbon film on a TEM grid. Heating the sample inside the microscope led first to reduction of the iron hydroxide and then movement of the resulting 'liquid-like' Fe particles across the carbon film, producing a trail of graphitic carbon. Glatzel *et al.*, used a similar approach but dispersed a sample of cellulose/$Fe(NO_3)_3$ on a TEM grid before heating *in situ* and recording video footage.[147] They observed very similar 'liquid-like' movement as the Fe/Fe_3C nanoparticles graphitized the sample.

6. Other graphitization catalysts

Although iron is the most studied catalyst for graphitization, many other elements are known to drive graphitization, with transition metals and especially iron, cobalt and nickel being the most efficient. From these three, the highest catalytic activity is normally found for iron, followed by cobalt and then nickel, as evidenced by the interplanar distance of the (002) planes and Raman intensity ratio between D and G bands of the resulting graphitic carbon.[139,167,191,249–251] The reason for this order is not clear, although some authors argue that is related to the number of electron vacancies in their d-shell orbitals.[82,139] Group VIII metals have a d-shell occupied by 6–10 electrons, with electron configurations of [Ar] $3d^64s^2$ for iron, [Ar] $3d^74s^2$ for cobalt and [Ar] $3d^84s^2$ for nickel, and the energy levels of their electronic configuration would only slightly change by accepting electrons from carbon, allowing for the formation of covalent bonds and the dissolution of carbon by the metal. According to this criterion, the catalytic activity of transition metals should have the order iron > cobalt > nickel, in agreement with experimental evidence.

An additional factor for explaining the high catalytic graphitization efficiency of iron may be related to carbon solubility at high temperatures and the ability to form metal carbides. While iron can form a stable carbide with carbon, nickel and cobalt carbides are metastable, due to their weaker carbon bonds, with the order of the enthalpy being: Fe–C < Co–C < Ni–C.[252] The maximum solubility of carbon in nickel is about 0.6 wt% at 1327 °C, while the maximum solubility of carbon in cobalt is 0.9 wt% at 1320 °C. For iron, the maximum solubility of carbon is 2.06 wt% at 1153 °C for the austenite (fcc) phase. This drops sharply to 0.02 wt% at 723 °C, where the transition to ferrite (bcc) iron occurs, due to the smaller interstitial positions in the ferrite lattice.[253] According to the maximum solubility, the order is again iron > cobalt > nickel for the catalytic activity of these three metals. The abrupt decrease in solubility upon the austenite to ferrite transition may also help explain the higher efficiency of iron as a graphitization catalyst from a classic solution-precipitation view.

Other elements have shown to be active catalysts for graphitization, as reviewed by Ōya and Marsh.[82] Ōya and Ōtani studied the graphitization of formaldehyde derived carbon at 2600–3000 °C by 10 wt% of Mg, Si, Ca, Cu, and Ge, which formed only graphitic carbon, and Al, Ti, V, Cr, Mn, Fe, Co, Ni, Mo and W, which formed both graphitic and turbostratic carbon.[83] In addition, B was found to markedly accelerate

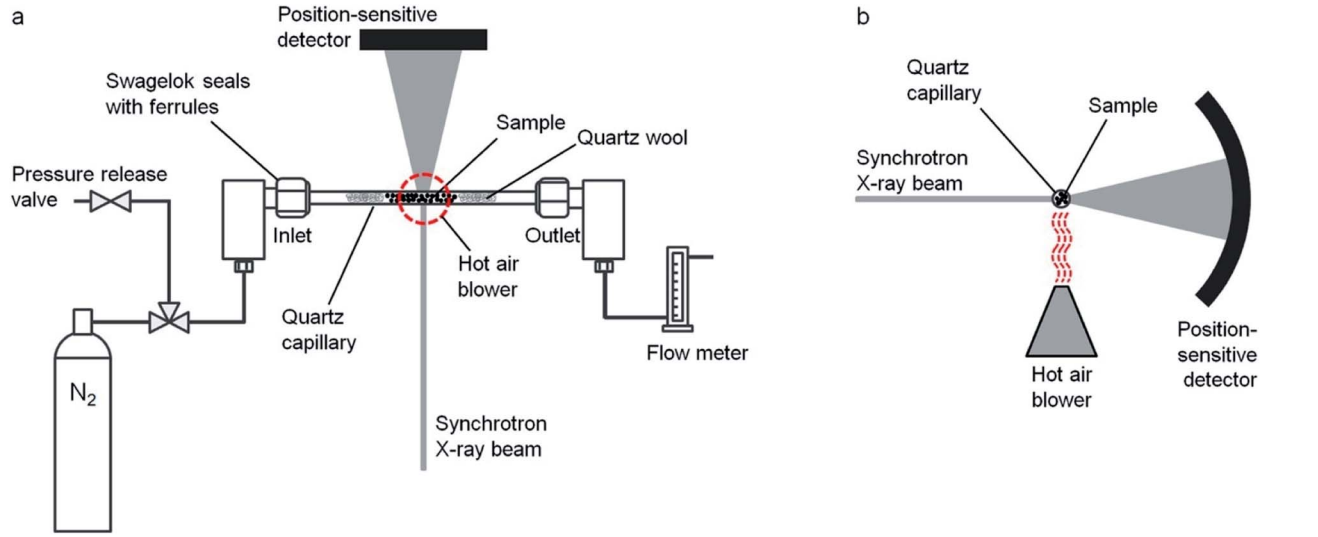

Fig. 17 Schematic of an experimental setup used to study pyrolysis of a gelatin/$Fe(NO_3)_3$ mixture *in situ* viewed from (a) the top and (b) the side. Figure reproduced with permission from ref. 223.

homogeneous graphitization, while Zn, Sn, Sb, Pb and Bi had no catalytic effect. Yokokawa *et al.* studied the graphitization of furfuryl alcohol-derived carbon at 1400–2300 °C by copper compounds and copper metal.[87] Weisweiler *et al.* used monolithic glass-like carbon crucibles filled with different metals and found Ni, Co, Fe, Pt, Mo, Cr and B to be highly effective in catalyzing graphitization, while Ag, Mg, Zn, Cd, Ge, Sn, Pb, Sb, Bi, Se, Te and Pd showed no reaction.[85] More recent works have studied the catalytic graphitization of rare earth elements,[254] yttrium,[255] manganese[121] and magnesium.[256]

7. Conclusions and perspective

Iron-catalyzed graphitization has the potential to be a scalable and economical route to carbons with complex graphitic structures. Natural graphite is listed by many governments as a critical material and there is a pressing need to identify routes to synthetic graphite materials. The appeal of iron-catalyzed graphitization is the simplicity. Organic matter is combined with an iron precursor and pyrolyzed in an inert atmosphere. For example, a complex network of graphitic nanotubes can be produced by heating a mixture of sawdust with iron nitrate. The method has proven to be extremely flexible, and authors have utilised a wide range of organic precursors and additional templates to produce carbons with diverse properties. One challenge that now needs to be addressed is how to translate this fascinating system into real-world applications. Iron-catalyzed graphitization appears to be scalable and flexible but there are very few examples of systematic or large-scale studies of this process. Without these, it is difficult to understand exactly how different precursors and heating conditions can be tuned to optimize the graphitic carbons towards certain applications. The few systematic studies that do exist have shown that it is possible to achieve dramatic variations in carbon structure through simple changes in precursors.[65,108]

Another challenge in iron-catalyzed graphitization is understanding the mechanism. It is still not clear why some organic precursors produce graphitic shells while others generate graphitic nanotubes. It is possible that the different precursors or conditions lead to different catalytic routes. This may relate to the chemical nature of the catalyst (Fe or Fe_3C) or to its physical state. When the catalyst does become mobile and produce graphitic nanotubes, it is not known why this movement is apparently random. If the movement of the catalyst particles could be understood and then controlled, it may be possible to further optimize the properties of the resulting carbons by introducing directional order between the nanotubes. On a simpler level, it is also important to gain a further understanding of how catalyst size influences the graphitization process and thus the porosity of the resulting materials. It is clear from all the examples in this paper that there is still much to be discovered in the field of iron-catalyzed graphitization. Increasingly sophisticated simulations, and synchrotron and electron microscopy experiments will undoubtedly offer insight into the nature of the catalytic process. However, there is also a lot of scope in simple, systematic experimental studies of different precursors and conditions.

Conflicts of interest

There are no conflicts to declare.

Acknowledgements

The authors acknowledge funding from the University of Birmingham (RDH), Leverhulme Trust under Grant No. RPG-2020-076 (ZS) and Consejería de Economía, Conocimiento, Empresas y Universidad, Junta de Andalucia, Spain, under Grant. No P20/01186 (JRR).

References

1 D. D. L. Chung, *Carbon Materials Science and Applications*, World Scientific Publishing Co., Singapore, 2019.
2 *Study on the EU's list of Critical Raw Materials*, 2020, https://ec.europa.eu/docsroom/documents/42883/attachments/1/translations/en/renditions/native, accessed November 2021.
3 G. J. Simandl, S. Paradis and C. Akam, in *Symposium on Strategic and Critical Materials Proceedings*, ed. G. J. Simandl and M. Neetz, British Columbia Geological Survey Paper, British Columbia Ministry of Energy and Mines, Victoria, British Columbia, 2015, vol. 2015-3, pp. 163–171.
4 X. Hu, X. Sun, S. J. Yoo, B. Evanko, F. Fan, S. Cai, C. Zheng, W. Hu and G. D. Stucky, *Nano Energy*, 2019, **56**, 828–839.
5 Y. Hu, J. O. Jensen, W. Zhang, L. N. Cleemann, W. Xing, N. J. Bjerrum and Q. Li, *Angew. Chem., Int. Ed.*, 2014, **53**, 3675–3679.
6 B. Li, L. Yang, C. Q. Wang, Q. P. Zhang, Q. C. Liu, Y. D. Li and R. Xhao, *Chemosphere*, 2017, **175**, 332–340.
7 M. Meyyappan, *J. Phys. D: Appl. Phys.*, 2009, **42**, 213001.
8 S. Iijima, *Nature*, 1991, **354**, 56–58.
9 T. Guo, P. Nikolaev, A. Thess, D. T. Colbert and R. E. Smalley, *Chem. Phys. Lett.*, 1995, **243**, 49–54.
10 M. M. Titirici, R. J. White, N. Brun, V. L. Budarin, D. S. Su, F. del Monte, J. H. Clark and M. J. MacLachlan, *Chem. Soc. Rev.*, 2015, **44**, 250–290.
11 *IUPAC Gold Book*, https://goldbook.iupac.org/html/C/C00894.html, accessed May 2021.
12 H. Darmstadt, C. Roy, S. Kaliaguine, G. Xu, M. Auger, A. Tuel and V. Ramaswamy, *Carbon*, 2000, **38**, 1279–1287.
13 A. C. Ferrari and J. Robertson, *Phys. Rev. B: Condens. Matter Mater. Phys.*, 2000, **61**, 14095.
14 F. R. Feret, *Analyst*, 1998, **123**, 595–600.
15 A. N. Popova, *Coke Chem.*, 2017, **60**, 361–365.
16 P. J. F. Harris, Z. Liu and K. Suenaga, *J. Phys.: Condens. Matter*, 2008, **20**, 362201.
17 J. M. Stratford, P. K. Allan, O. Pecher, P. A. Chater and C. P. Grey, *Chem. Commun.*, 2016, **52**, 12430–12433.
18 A. S. Marriott, A. J. Hunt, E. Bergström, K. Wilson, V. L. Budarin, J. Thomas-Oates, J. H. Clark and R. Brydson, *Carbon*, 2014, **67**, 514–524.
19 J.-B. Donnet, R. C. Bansal and M.-J. Wang, *Carbon Black*, Marcel Dekker, Inc., New York, 1993.
20 W. Long, B. Fang, A. Ignaszak, Z. Wu, Y.-J. Wang and D. Wilkinson, *Chem. Soc. Rev.*, 2017, **46**, 7176–7190.
21 X. Dou, I. Hasa, D. Saurel, C. Vaalma, L. Wu, D. Buchholz, D. Bresser, S. Komaba and S. Passerini, *Mater. Today*, 2019, **23**, 87–104.
22 Y. Li, Y.-S. Hu, H. Li, L. Chen and X. Huang, *J. Mater. Chem. A*, 2016, **4**, 96–104.
23 E. Fitzer, K.-H. Köchling, H. P. Boehm and H. Marsh, *Pure Appl. Chem.*, 1995, **67**, 473–506.
24 H. Pan, M. Pruski, B. C. Gerstein, F. Li and J. S. Lannin, *Phys. Rev. B: Condens. Matter Mater. Phys.*, 1991, **44**, 6741–6745.
25 M. Monthioux, *Carbon*, 2020, **160**, 405–406.
26 A. Ghemes, J. Muramatsu, Y. Minami, M. Okada, Y. Inoue and H. Mimura, *Journal of Advanced Research in Physics*, 2012, **3**, 011207.
27 X. Xie, L. Ju, X. Feng, Y. Sun, R. Zhou, K. Liu, S. Fan, Q. Li and K. Jiang, *Nano Lett.*, 2009, **9**, 2565–2570.
28 Y. Saito and T. Yoshikawa, *J. Cryst. Growth*, 1993, **134**, 154–156.
29 W. Fan, Z. Li, C. You, X. Zong, X. Tian, S. Miao, T. Shu, C. Li and S. Liao, *Nano Energy*, 2017, **37**, 187–194.
30 D. Pech, M. Brunet, H. Durou, P. Huang, V. Mochalin, Y. Gogotsi, P.-L. Taberna and P. Simon, *Nat. Nanotechnol.*, 2010, **5**, 651–654.
31 W. Lian, H. Song, X. Chen, L. Li, J. Huo, M. Zhao and G. Wang, *Carbon*, 2008, **46**, 525–530.
32 M. E. Plonska-Brzezinska, *ChemNanoMat*, 2019, **5**, 568–580.
33 R. Van Noorden, *Nature*, 2011, **469**, 14–16.
34 A. Bianco, H.-M. Cheng, T. Enoki, Y. Gogotsi, R. H. Hurt, N. Koratkar, T. Kyotani, M. Monthioux, C. R. Park, J. M. D. Tascon and J. Zhang, *Carbon*, 2013, **65**, 1–6.
35 R. E. Franklin, *Proc. R. Soc. London, Ser. A*, 1951, **209**, 196–218.
36 P. J. F. Harris, *J. Mater. Sci.*, 2013, **48**, 565–577.
37 A. C. Forse, C. Merlet, P. K. Allan, E. K. Humphreys, J. M. Griffin, M. Aslan, M. Zeiger, V. Pressesr, Y. Gogotsi and C. P. Grey, *Chem. Mater.*, 2015, **27**, 6848–6857.
38 S. J. Townsend, T. J. Lenosky, D. A. Muller, C. S. Nichols and V. Elser, *Phys. Rev. Lett.*, 1992, **69**, 921–924.
39 A. P. Terzyk, S. Furmaniak, P. J. F. Harris, P. A. Gauden, J. Włoch, P. Kowalczyk and G. Rychlicki, *Phys. Chem. Chem. Phys.*, 2007, **9**, 5919–5927.
40 A. R. Payne and R. E. Whittaker, *Composites*, 1970, **1**, 203–214.
41 D. D. L. Chung, *Carbon Fiber Composites*, Butterworth-Heinemann, Newton, MA, 1994.
42 H. Marsh and F. Rodríguez-Reinoso, *Activated Carbon*, Elsevier, Oxford, 2006.
43 M. R. Benzigar, S. N. Talapaneni, S. Joseph, K. Ramadass, G. Singh, J. Scaranto, U. Ravon, K. Al-Bahily and A. Vinu, *Chem. Soc. Rev.*, 2018, **47**, 2680–2721.
44 L. Wang and X. Hu, *Chem.–Asian J.*, 2018, **13**, 1518–1529.
45 M. M. Sabzehmeidani, S. Mahnaee, M. Ghaedi, H. Heidari and V. A. L. Roy, *Mater. Adv.*, 2021, **2**, 598–627.
46 M. Shao, Q. Chang, J.-P. Dodelet and R. Chenitz, *Chem. Rev.*, 2016, **116**, 3594–3657.
47 C. W. B. Bezerra, L. Zhang, K. Lee, H. Liu, A. L. B. Marques, E. P. Marques, H. Wang and J. Zhang, *Electrochim. Acta*, 2008, **53**, 4937–4951.
48 H. Tan, J. Tang, J. Kim, Y. V. Kaneti, Y.-M. Kang, Y. Sugahara and Y. Yamauchi, *J. Mater. Chem. A*, 2019, **7**, 1380–1393.
49 Y. Nishi, *Chem. Rec.*, 2001, **1**, 406–413.
50 J. Asenbauer, T. Eisenmann, M. Kuenzel, A. Kazzazi, Z. Chen and D. Bresser, *Sustainable Energy Fuels*, 2020, **4**, 5387–5416.

51 A. Gomez-Martin, J. Martinez-Fernandez, M. Ruttert, A. Heckmann, M. Winter, T. Placke and J. Ramirez-Rico, *ChemSusChem*, 2018, **11**, 2776–2787.
52 W.-J. Liu, H. Jiang and H.-Q. Yu, *Energy Environ. Sci.*, 2019, **12**, 1751–1779.
53 C. Liedel, *ChemSusChem*, 2020, **13**, 2110–2141.
54 A. Gutiérrez-Pardo, J. Ramírez-Rico, R. Cabezas-Rodríguez and J. Martínez-Fernández, *J. Power Sources*, 2015, **278**, 18–26.
55 Y. Li, J. Hu, Z. Wang, K. Yang, W. Huang, B. Cao, Z. Li, W. Zhang and F. Pan, *ACS Appl. Mater. Interfaces*, 2019, **11**, 24164–24171.
56 N. Wang, Q. Liu, B. Sun, J. Gu, B. Yu, W. Zhang and D. Zhang, *Sci. Rep.*, 2018, **8**, 9934.
57 V. Gupta and T. A. Saleh, *Environ. Sci. Pollut. Res.*, 2013, **20**, 2828–2843.
58 J. Xu, Z. Cao, Y. Zhang, Z. Yuan, Z. Lou, X. Xu and X. Wang, *Chemosphere*, 2018, **195**, 351–364.
59 W. Chen, L. Duan and D. Zhu, *Environ. Sci. Technol.*, 2007, **41**, 8295–8300.
60 H. J. Wang, A. L. Zhou, F. Peng, H. Yu and J. Yang, *J. Colloid Interface Sci.*, 2007, **316**, 277–283.
61 S. A. C. Carabineiro, T. Thavorn-amornsri, M. F. R. Pereira, P. Serp and J. L. Figueiredo, *Catal. Today*, 2012, **186**, 29–34.
62 L. Ji, W. Chen, L. Duan and D. Zhu, *Environ. Sci. Technol.*, 2009, **43**, 2322–2327.
63 M. J. Sweetman, S. May, N. Mebberson, P. Pendleton, K. Vasilev, S. E. Plush and J. D. Hayball, *J. Carbon Res.*, 2017, **3**, 18.
64 S. C. Smith and D. F. Rodrigues, *Carbon*, 2015, **91**, 122–143.
65 J. Hoekstra, A. M. Beale, F. Soulimani, M. Versluijs-Helder, D. van de Kleut, M. Koelewijn, J. W. Geus and L. W. Jenneskens, *Carbon*, 2016, **107**, 248–260.
66 R. D. Hunter, J. Davies, S. J. A. Hérou, A. Kulak and Z. Schnepp, *Philos. Trans. R. Soc., A*, 2021, **379**, 20200336.
67 H. Valladas, *Meas. Sci. Technol.*, 2003, **14**, 1487–1492.
68 P. Harris, *Interdiscip. Sci. Rev.*, 1999, **24**, 301–306.
69 M. J. Antal and M. Grønli, *Ind. Eng. Chem. Res.*, 2003, **42**, 1619–1640.
70 J. Lehmann and S. Joseph, *Biochar for Environmental Management Science and Technology*, Earthscan, London, 2009.
71 Z. Heidarinejad, M. H. Dehghani, M. Heidari, G. Javedan, I. Ali and M. Sillanpää, *Environ. Chem. Lett.*, 2020, **18**, 393–415.
72 N. Arora and N. N. Sharma, *Diamond Relat. Mater.*, 2014, **50**, 135–150.
73 N. I. Alekseyev and G. A. Dyuzhev, *Carbon*, 2003, **41**, 1343–1348.
74 Y. Saito, T. Nakahira and S. Uemura, *J. Phys. Chem. B*, 2003, **107**, 931–934.
75 R. Hu, T. Furukawa, X. Wang and M. Nagatsu, *Appl. Surf. Sci.*, 2017, **416**, 731–741.
76 J. Prasek, J. Drbohlavova, J. Chomoucka, J. Hubalek, O. Jasek, V. Adam and R. Kisek, *J. Mater. Chem.*, 2011, **21**, 15872–15884.
77 M. Kokarneswaran, P. Selvaraj, T. Ashokan, S. Perumal, P. Sellappan, K. D. Murugan, S. Ramalingam, N. Mohan and V. Chandrasekaran, *Sci. Rep.*, 2020, **10**, 19786.
78 M. Reibold, P. Paufler, A. A. Levin, W. Kochmann, N. Pätzke and D. C. Meyer, *Nature*, 2006, **444**, 286.
79 E. Charon, J.-N. Rouzaud and J. Aléon, *Carbon*, 2014, **66**, 178–190.
80 H. Marsh and A. P. Warburton, *J. Appl. Chem.*, 1970, **20**, 133–142.
81 E. G. Acheson, *US Pat.*, 568323 (1896), 616974 (1899) and 645285 (1900).
82 A. Oya and H. Marsh, *J. Mater. Sci.*, 1982, **17**, 309–322.
83 A. Oya and S. Otani, *Carbon*, 1979, **17**, 131–137.
84 S. M. Irving and P. L. Walker, *Carbon*, 1967, **5**, 399–400.
85 W. Weisweiler, N. Subramanian and B. Terwiesch, *Carbon*, 1971, **9**, 755–761.
86 T. Britt and P. C. Pistorius, *Metall. Mater. Trans. B*, 2021, **52**, 1–5.
87 C. Yokokawa, K. Hosokawa and Y. Takegami, *Carbon*, 1966, **4**, 459–465.
88 S. Gupta, V. Sahajwalla, J. Burgo, P. Chaubal and T. Youmans, *Metall. Mater. Trans. B*, 2005, **36**, 385–394.
89 K. Li, H. Li, M. Sun, J. Zhang, H. Zhang, S. Ren and M. Barati, *Energy Fuels*, 2019, **33**, 10941–10952.
90 H. Li, H. Zhang, K. Li, J. Zhang, M. Sun and B. Su, *Fuel*, 2020, **279**, 118531.
91 P. L. Walker, J. F. Rakszawski and G. R. Imperial, *J. Phys. Chem.*, 1959, **63**, 133–140.
92 W. R. Davis, R. Slawson and G. R. Rigby, *Nature*, 1953, **171**, 756.
93 W. R. Ruston, M. Warzee, J. Hennaut and J. Waty, *Carbon*, 1969, **7**, 47–57.
94 H. P. Boehm, *Carbon*, 1973, **11**, 583–590.
95 A. Oberlin and M. Endo, *J. Cryst. Growth*, 1976, **32**, 335–349.
96 M. José-Yacamán, M. Miki-Yoshida, L. Rendón and J. G. Santiesteban, *Appl. Phys. Lett.*, 1993, **62**, 657.
97 H. Marsh, D. Crawford and D. W. Taylor, *Carbon*, 1983, **21**, 81–87.
98 J. Ozaki, M. Mitsui and Y. Nishiyama, *Carbon*, 1998, **36**, 131–135.
99 J. Yang and S. Zuo, *Diamond Relat. Mater.*, 2019, **95**, 1–4.
100 M. Sevilla, C. Sanchís, T. Valdés-Solís, E. Morallón and A. B. Fuertes, *Carbon*, 2008, **46**, 931–939.
101 L. Chen, Z. Wang, C. He, N. Zhao, C. Shi, E. Liu and J. Li, *ACS Appl. Mater. Interfaces*, 2013, **5**, 9537–9545.
102 C. Defilippi, M. O. A. Mukadam, S. A. Nicolae, M. R. Lees and C. Giordano, *Materials*, 2019, **12**, 323.
103 M. N. Obrovac, X. Zhao, L. T. Burke and R. A. Dunlap, *Electrochem. Commun.*, 2015, **60**, 221–224.
104 M. J. Xie, J. Yang, J. Y. Liang, X. F. Guo and W. P. Ding, *Carbon*, 2014, **77**, 215–225.
105 J. Hoekstra, A. M. Beale, F. Soulimani, M. Versluijs-Helder, J. W. Geus and L. W. Jenneskens, *New J. Chem.*, 2015, **39**, 6593–6601.
106 H. Niu, Y. Wang, X. Zhang, Z. Meng and Y. Cai, *ACS Appl. Mater. Interfaces*, 2012, **4**, 286–295.

107 Z. Tian, C. Wang, J. Yue, X. Zhang and L. Ma, *Catal. Sci. Technol.*, 2019, **9**, 2728–2741.
108 R. D. Hunter, J. L. Rowlandson, G. J. Smales, B. R. Pauw, V. P. Ting, A. Kulak and Z. Schnepp, *Mater. Adv.*, 2020, **1**, 3281–3291.
109 R. Atchudan, S. Perumal, T. N. J. I. Edison and Y. R. Lee, *Mater. Lett.*, 2016, **166**, 145–149.
110 Z. Cao, M. Qin, C. Zuo, Y. Gu and B. Jia, *J. Colloid Interface Sci.*, 2017, **491**, 55–63.
111 S. Juvanen, A. Sarapuu, S. Vlassov, M. Kook, V. Kisand, M. Käärik, A. Treshchalov, J. Aruväli, J. Kozlova, A. Tamm, J. Leis and K. Tammeveski, *ChemElectroChem*, 2021, **8**, 2288–2297.
112 I.-A. Choi, D.-H. Kwak, S.-B. Han, J.-Y. Park, H.-S. Park, K.-B. Ma, D.-H. Kim, J.-E. Won and K.-W. Park, *Appl. Catal., B*, 2017, **211**, 235–244.
113 J. J. Shi, X. M. Hu, M. R. Madsen, P. Lamagni, E. T. Bjerglund, S. U. Pedersen, T. Skrydstrup and K. Daasbjerg, *ACS Appl. Nano Mater.*, 2018, **1**, 3608–3615.
114 H. Khani, N. S. Grundish, D. O. Wipf and J. B. Goodenough, *Adv. Energy Mater.*, 2020, **10**, 1903215.
115 M. Xiao, J. Zhu, L. Feng, C. Liu and W. Xing, *Adv. Mater.*, 2015, **27**, 2521–2527.
116 C. W. Huang, L. C. Hsu and Y. Y. Li, *Nanotechnology*, 2006, **17**, 4629–4634.
117 Z. Tang, Y. Song, X. He and J. Yang, *Mater. Lett.*, 2012, **89**, 330–332.
118 K. Inomata and Y. Otake, *Microporous Mesoporous Mater.*, 2011, **143**, 60–65.
119 G. Hasegawa, K. Kanamori and K. Nakanishi, *Mater. Lett.*, 2012, **76**, 1–4.
120 N. I. Maksimova, O. P. Krivoruchko, G. Mestl, V. I. Zaikovskii, A. L. Chuvilin, A. N. Salanov and E. B. Burgina, *J. Mol. Catal. A: Chem.*, 2000, **158**, 301–307.
121 M. Sevilla and A. B. Fuertes, *Carbon*, 2006, **44**, 468–478.
122 J. J. Li, Y. Liang, B. J. Dou, C. Y. Ma, R. J. Lu, Z. P. Hao, Q. Xie, Z. Q. Luan and K. Li, *Mater. Chem. Phys.*, 2013, **138**, 484–489.
123 A. M. Wang, J. W. Ren, B. F. Shi, G. Z. Lu and Y. Q. Wang, *Microporous Mesoporous Mater.*, 2012, **151**, 287–292.
124 J. S. Li, J. Gu, H. J. Li, Y. Liang, Y. X. Hao, X. Y. Sun and L. J. Wang, *Microporous Mesoporous Mater.*, 2010, **128**, 144–149.
125 J. I. Ozaki, K. Nozawa, K. Yamada, Y. Uchiyama, Y. Yoshimoto, A. Furuichi, T. Yokoyama, A. Oya, L. J. Brown and J. D. Cashion, *J. Appl. Electrochem.*, 2006, **36**, 239–247.
126 C. G. Renda, R. Bertholdo, T. Venancio, A. P. Luz, V. C. Pandolfelli and A. A. Lucas, *Ceram. Int.*, 2019, **45**, 12196–12204.
127 B. Zhang, C. Liu, W. Kong and C. Qi, *Frontiers of Materials Science*, 2016, **10**, 147–156.
128 J. Qi, L. H. Jiang, Q. W. Tang, S. Zhu, S. L. Wang, B. L. Yi and C. Q. Sun, *Carbon*, 2012, **50**, 2824–2831.
129 A. Abdelwahab, J. Castelo-Quibén, J. F. Vivo-Vilches, M. Pérez-Cadenas, F. J. Maldonado-Hódar, F. Carrasco-Marin and A. F. Pérez-Cadenas, *Nanomaterials*, 2018, **8**, 266.
130 A. Chen, Y. Yu, T. Xing, R. Wang, Y. Zhang and Q. Li, *J. Mater. Sci.*, 2015, **50**, 5578–5582.
131 M. M. Gaikwad, M. Kakunuri and C. S. Sharma, *Mater. Today Commun.*, 2019, **20**, 100569.
132 W. Kicinski, M. Norek and M. Bystrzejewski, *J. Phys. Chem. Solids*, 2013, **74**, 101–109.
133 Y.-H. Chung and S. Jou, *Mater. Chem. Phys.*, 2005, **92**, 256–259.
134 F. Cesano, M. M. Rahman, F. Bardelli, A. Damin and D. Scarano, *ChemistrySelect*, 2016, **1**, 2536–2541.
135 S. Zhu, Y. Wu, Q. Chen, Z. Yu, C. Wang, S. Jin, Y. Ding and G. Wu, *Green Chem.*, 2006, **8**, 325–327.
136 M. Egal, T. Budtova and P. Navard, *Biomacromolecules*, 2007, **8**, 2282–2287.
137 A. Huidobro, A. C. Pastor and F. Rodríguez-Reinoso, *Carbon*, 2001, **39**, 389–398.
138 A. Solak and P. Rutkowski, *J. Mater. Cycles Waste Manage.*, 2014, **16**, 491–499.
139 Q. C. Yan, J. H. Li, X. F. Zhang, E. Hassan, C. J. Wang, J. L. Zhang and Z. Y. Cai, *J. Nanopart. Res.*, 2018, **20**, 223.
140 Q. G. Yan, J. H. Li, X. F. Zhang, J. L. Zhang and Z. Y. Cai, *Nanomater. Nanotechnol.*, 2018, **8**, 1–12.
141 X. F. Zhang, Q. G. Yan, J. H. Li, I. W. Chu, H. Toghiani, Z. Y. Cai and J. L. Zhang, *Polymers*, 2018, **10**, 183.
142 G. Daniel, T. Kosmala, F. Brombin, M. Mazzucato, A. Facchin, M. C. Dalconi, D. Badocco, P. Pastore, G. Granozzi and C. Durante, *Catalysts*, 2021, **11**, 390.
143 S. W. Zhang, M. Y. Zeng, J. X. Li, J. Li, J. Z. Xu and X. K. Wang, *J. Mater. Chem. A*, 2014, **2**, 4391–4397.
144 A. E. Danks, M. J. Hollamby, B. Hammouda, D. C. Fletcher, F. Johnston-Banks, S. E. Rogers and Z. Schnepp, *J. Mater. Chem. A*, 2017, **5**, 11644–11651.
145 Z. Schnepp, Y. Zhang, M. J. Hollamby, B. R. Pauw, M. Tanaka, Y. Matsushita and Y. Sakka, *J. Mater. Chem. A*, 2013, **1**, 13576–13581.
146 J. Hoekstra, A. M. Beale, F. Soulimani, M. Versluijs-Helder, J. W. Geus and L. W. Jenneskens, *J. Phys. Chem. C*, 2015, **119**, 10653–10661.
147 S. Glatzel, Z. Schnepp and C. Giordano, *Angew. Chem., Int. Ed.*, 2013, **52**, 2355–2358.
148 K. Lotz, A. Wutscher, H. Dudder, C. M. Berger, C. Russo, K. Mukherjee, G. Schwaab, M. Havenith and M. Muhler, *ACS Omega*, 2019, **4**, 4448–4460.
149 J. Hoekstra, M. Versluijs-Helder, E. J. Vlietstra, J. W. Geus and L. W. Jenneskens, *ChemSusChem*, 2015, **8**, 985–989.
150 S. Shi, W. Che, K. Liang, C. Xia and D. Zhang, *J. Anal. Appl. Pyrolysis*, 2015, **115**, 1–6.
151 A. N. Prusov, S. M. Prusova, A. G. Zakharov, A. V. Bazanov and V. K. Ivanov, *Fibre Chem.*, 2018, **50**, 154–160.
152 S. Xia, N. Cai, W. Lu, H. Zhou, H. Xiao, X. Chen, Y. Chen, H. Yang, X. Wang, S. Wang and H. Chen, *J. Cleaner Prod.*, 2021, **329**, 129735.
153 Q. Yan, X. Zhang, J. Li, E. Hassan, C. Wang, J. Zhang and Z. Cai, *J. Mater. Sci.*, 2018, **53**, 8020–8029.
154 X. Zhang, Q. Yan, J. Li, J. Zhang and Z. Cai, *Materials*, 2018, **11**, 139.
155 S. T. Neeli and H. Ramsurn, *Carbon*, 2018, **134**, 480–490.

156 Z. Schnepp, Y. Zhang, M. J. Hollamby, B. R. Pauw, M. Tanaka, Y. Matsushita and Y. Sakka, *J. Mater. Chem. A*, 2013, **1**, 13576–13581.
157 J. Zhao, Y. Liu, X. Quan, S. Chen, H. Yu and H. Zhao, *Appl. Surf. Sci.*, 2017, **396**, 986–993.
158 Q. Chen, X. Tan, Y. Liu, S. Liu, M. Li, Y. Gu, P. Zhang, S. Ye, Z. Yang and Y. Yang, *J. Mater. Chem. A*, 2020, **8**, 5773–5811.
159 S. Sotiropoulou, Y. Sierra-Sastre, S. S. Mark and C. A. Batt, *Chem. Mater.*, 2008, **20**, 821–834.
160 E. Thompson, A. E. Danks, L. Bourgeois and Z. Schnepp, *Green Chem.*, 2015, **17**, 551–556.
161 W.-J. Liu, K. Tian, Y.-R. He, H. Jiang and H.-Q. Yu, *Environ. Sci. Technol.*, 2014, **48**, 13951–13959.
162 W.-J. Liu, F.-X. Zeng, H. Jiang and H.-Q. Yu, *Bioresour. Technol.*, 2011, **102**, 3471–3479.
163 S. Zhang, Y. Su, S. Zhu, H. Zhang and Q. Zhang, *J. Anal. Appl. Pyrolysis*, 2018, **135**, 22–31.
164 Z. Xu, Y. Zhou, Z. Sun, D. Zhang, Y. Huang, S. Gu and W. Chen, *Chemosphere*, 2020, **241**, 125120.
165 Z. Xu, Z. Sun, Y. Zhou, W. Chen, T. Zhang, Y. Huang and D. Zhang, *Colloids Surf., A*, 2019, **582**, 123934.
166 J. Bedia, M. Peñas-Garzón, A. Gómez-Avilés, J. J. Rodriguez and C. Belver, *J. Carbon Res.*, 2020, **6**, 21.
167 M. Sevilla, C. Sanchís, T. Valdés-Solís, E. Morallón and A. B. Fuertes, *J. Phys. Chem. C*, 2007, **111**, 9749–9756.
168 A. Gomez-Martin, A. Gutierrez-Pardo, J. Martinez-Fernandez and J. Ramirez-Rico, *Fuel Process. Technol.*, 2020, **199**, 106279.
169 L. Ma, Y. Xu, Y. Liu, H. Zhang, J. Yao, N. Li, C. M. Li, W. Zhou and J. Jiang, *ACS Sustainable Chem. Eng.*, 2019, **7**, 17919–17928.
170 Y. Gong, D. Li, C. Luo, Q. Fu and C. Pan, *Green Chem.*, 2017, **19**, 4132–4140.
171 L. Sun, C. Tian, M. Li, X. Meng, L. Wang, R. Wang, J. Yin and H. Fu, *J. Mater. Chem. A*, 2013, **1**, 6462–6470.
172 Q. Liu, J. Gu, W. Zhang, Y. Miyamoto, Z. Chen and D. Zhang, *J. Mater. Chem.*, 2012, **22**, 21183–21188.
173 Y. Liu, J. Ruan, S. Sang, Z. Zhou and Q. Wu, *Electrochim. Acta*, 2016, **215**, 388–397.
174 F. Wu, R. Huang, D. Mu, B. Wu and Y. Chen, *Electrochim. Acta*, 2016, **187**, 508–516.
175 X. Li, E. Cui, Z. Xiang, L. Yu, J. Xiong, F. Pan and W. Lu, *Colloids Surf., A*, 2020, **819**, 152952.
176 L. Chen, T. Ji, L. Mu, Y. Shi, L. Brisbin, Z. Guo, M. A. Khan, D. P. Young and J. Zhu, *RSC Adv.*, 2016, **6**, 2259–2269.
177 Z. Yan, C. Dai, M. Zhang, X. Lu, X. Zhao and J. Xie, *Int. J. Hydrogen Energy*, 2019, **44**, 4090–4101.
178 Y. Cai, Y. Luo, H. Dong, X. Zhao, Y. Xiao, Y. Liang, H. Hu, Y. Liu and M. Zheng, *J. Power Sources*, 2017, **353**, 260–269.
179 I. Major, J. M. Pin, E. Behazin, A. Rodriguez-Uribe, M. Misra and A. Mohanty, *Green Chem.*, 2018, **20**, 2269–2278.
180 E. Petala, Y. Georgiou, V. Kostas, K. Dimos, M. A. Karakassides, Y. Deligiannakis, C. Aparicio, J. Tuček and R. Zbořil, *ACS Sustainable Chem. Eng.*, 2017, **5**, 5782–5792.
181 X. Zhang, H. Li, K. Zhang, Q. Wang, B. Qin, Q. Cao and L. Jin, *J. Electrochem. Soc.*, 2018, **165**, A2084–A2092.
182 S. Xia, K. Li, H. Xiao, N. Cai, Z. Dong, C. Xu, Y. Chen, H. Yang, X. Tu and H. Chen, *Bioresour. Technol.*, 2019, **287**, 121444.
183 W. Tian, Q. Gao, Y. Tan and Z. Li, *Carbon*, 2017, **119**, 287–295.
184 M. A. Ahsan, A. R. Puente Santiago, A. Rodriguez, V. Maturano-Rojas, B. Alvarado-Tenorio, R. Bernal and J. C. Noveron, *J. Cleaner Prod.*, 2020, **275**, 124141.
185 S. Xia, N. Cai, J. Wu, H. Xiao, J. Hu, X. Chen, Y. Chen, H. Yang, X. Wang and H. Chen, *Fuel Process. Technol.*, 2020, **209**, 106543.
186 K. Suzuki, Y. Saito, N. Okazaki and T. Suzuki, *Sci. Rep.*, 2020, **10**, 12131.
187 A. S. Kamal, N. H. Jabarullah and R. Othman, *Mater. Today: Proc.*, 2020, **31**, 211–216.
188 J. He, D. Zhang, Y. Wang, J. Zhang, B. Yang, H. Shi, K. Wang and Y. Wang, *Appl. Surf. Sci.*, 2020, **515**, 146020.
189 B. S. Purwasasmita, F. Tafwidli and R. Septawendar, *J. Aust. Ceram. Soc.*, 2013, **49**, 119–126.
190 X. Zhang, K. Zhang, H. Li, Q. Cao, L. Jin and P. Li, *J. Power Sources*, 2017, **344**, 176–184.
191 M. Sevilla, C. Salinas Martínez-de Lecca, T. Valdés-Solís, E. Morallón and A. B. Fuertes, *Phys. Chem. Chem. Phys.*, 2008, **10**, 1433–1442.
192 Z. H. Li, H. Y. Zhang, H. P. Zhu, L. Q. Li and H. Y. Liao, *J. Mater. Sci.*, 2016, **51**, 5676–5684.
193 A. Leonhardt, M. Ritschel, D. Elefant, N. Mattern, K. Biedermann, S. Hampel, C. Müller, T. Gemming and B. Büchner, *J. Appl. Phys.*, 2005, **98**, 074315.
194 Z. M. Sheng, M. H. Hu, Z. Y. Dai, C. Y. Hong, C. K. Chang, Q. Z. Chen and X. J. Chang, *Microporous Mesoporous Mater.*, 2016, **234**, 224–229.
195 J. N. Wang, L. Zhang, J. J. Niu, F. Yu, Z. M. Sheng, Y. Z. Zhao, H. Chang and C. Pak, *Chem. Mater.*, 2007, **19**, 453–459.
196 A. O. Baskakov, I. S. Lyubutin, S. S. Starchikov, V. A. Davydov, L. F. Kulikova, T. B. Egorova and V. N. Agafonov, *Inorg. Chem.*, 2018, **57**, 14895–14903.
197 K. T. Lee, X. Ji, M. Rault and L. F. Nazar, *Angew. Chem., Int. Ed.*, 2009, **48**, 5661–5665.
198 J. Song, M. Sun, Q. Chen, J. Wnag, G. Zhang and Z. Xue, *J. Phys. D: Appl. Phys.*, 2004, **37**, 5–9.
199 S. S. Starchikov, V. A. Zayakhanov, A. L. Vasiliev, S. Lyubutin, A. O. Baskakov, Y. A. Nikiforova, K. O. Funtov, M. V. Lyubutina, L. F. Kulikova, V. N. Agafonov and V. A. Davydov, *Carbon*, 2021, **178**, 708–717.
200 V. Jourdain and C. Bichara, *Carbon*, 2013, **58**, 2–39.
201 J.-P. Tessonier and D. S. Su, *ChemSusChem*, 2011, **4**, 824–847.
202 H. Dai, A. G. Rinzler, P. Nikolaev, A. Thess, D. T. Colbert and R. E. Smalley, *Chem. Phys. Lett.*, 1996, **260**, 471–475.
203 A. J. Page, Y. Ohta, S. Irle and K. Morokuma, *Acc. Chem. Res.*, 2010, **43**, 1375–1385.
204 M. A. Ribas, F. Ding, P. B. Balbuena and B. I. Yakobson, *J. Chem. Phys.*, 2009, **131**, 224501.

205 C. T. Wirth, B. C. Bayer, A. D. Gamalski, S. Esconjauregui, R. S. Weatherup, C. Ducati, C. Baehtz, J. Robertson and S. Hofmann, *Chem. Mater.*, 2012, **24**, 4633–4640.
206 S. Hofmann, R. Sharma, C. Ducati, G. Du, C. Mattevi, C. Cepek, M. Cantoro, S. Pisana, A. Parvez, F. Cervantes-Sodi, A. C. Ferrari, R. Dunin-Borkowski, S. Lizzit, L. Petaccia, A. Goldoni and J. Robertson, *Nano Lett.*, 2007, **7**, 602–608.
207 F. Ding, A. Rosen, E. E. B. Campbell, L. K. L. Falk and K. Bolton, *J. Phys. Chem. B*, 2006, **110**, 7666–7670.
208 Z. D. Zhang, J. G. Zheng, I. Skorvanek, G. H. Wen, J. Kovac, F. W. Wang, J. L. Yu, Z. J. Li, X. L. Dong, S. R. Jin, W. Liu and X. X. Zhang, *J. Phys.: Condens. Matter*, 2001, **13**, 1921–1929.
209 F. Ding, K. Bolton and A. Rosén, *J. Phys. Chem. B*, 2004, **108**, 17369–17377.
210 C. L. Cheung, A. Kurtz, H. Park and C. M. Lieber, *J. Phys. Chem. B*, 2002, **106**, 2429–2433.
211 F. Ding, A. Rosen and K. Bolton, *J. Chem. Phys.*, 2004, **121**, 2775–2779.
212 Z. Yu, D. Chen, B. Tøtdal and A. Holmen, *Catal. Today*, 2005, **100**, 261–267.
213 S. Hofmann, G. Csanyi, A. C. Ferrari, M. C. Payne and J. Robertson, *Phys. Rev. Lett.*, 2005, **95**, 036101.
214 A. A. Puretzky, D. B. Geohegan, S. Jesse, I. N. Ivanov and G. Eres, *Appl. Phys. A: Mater. Sci. Process.*, 2005, **81**, 223–240.
215 Y. Wang, B. Li, P. S. Ho, Z. Yao and L. Shi, *Appl. Phys. Lett.*, 2006, **89**, 183113.
216 Z. He, J.-L. Maurice, A. Gohier, C. S. Lee, D. Pribat and C. S. Cojocaru, *Chem. Mater.*, 2011, **23**, 5379–5387.
217 M. Lin, J. P. Y. Tan, C. Boothroyd, K. P. Loh, E. S. Tok and Y.-L. Foo, *Nano Lett.*, 2007, **7**, 2234–2238.
218 F. Ding, K. Bolton and A. Rosén, *J. Electron. Mater.*, 2006, **35**, 207–210.
219 T. Ichihashi, M. Ishida, Y. Ochiai and J. Fujita, *J. Vac. Sci. Technol., B: Microelectron. Nanometer Struct.–Process., Meas., Phenom.*, 2004, **22**, 3221–3223.
220 C. T. Wirth, S. Hofmann and J. Robertson, *Diamond Relat. Mater.*, 2009, **18**, 940–945.
221 H. Yoshida, S. Takeda, T. Uchiyama, H. Kohno and Y. Homma, *Nano Lett.*, 2008, **8**, 2082–2086.
222 A. Gomez-Martin, Z. Schnepp and J. Ramirez-Rico, *Chem. Mater.*, 2021, **33**, 3087–3097.
223 Z. Schnepp, A. E. Danks, M. J. Hollamby, B. R. Pauw, C. A. Murray and C. C. Tang, *Chem. Mater.*, 2015, **27**, 5094–5099.
224 A. Mehmood, J. Pampel, G. Ali, H. Y. Ha, F. Ruiz-Zepeda and T.-P. Fellinger, *Adv. Energy Mater.*, 2018, **8**, 1701771.
225 D. Menga, J. L. Low, Y.-S. Li, I. Arčon, B. Koyotürk, F. Wagner, F. Ruiz-Zepeda, M. Gaberšček, B. Paulus and T.-P. Fellinger, *J. Am. Chem. Soc.*, 2021, **143**, 18010–18019.
226 J. Wu, Z. Pan, Y. Zhang, B. Wang and H. Peng, *J. Mater. Chem. A*, 2018, **6**, 12932–12944.
227 G. Li, J. Yu, W. Yu, L. Yang, X. Zhang, X. Liu, H. Liu and W. Zhou, *Small*, 2020, **16**, 2001980.
228 S. S. Shah, S. M. A. Nayem, N. Sultana, A. J. S. Ahammad and M. A. Aziz, *ChemSusChem*, 2022, **15**, e202101282.
229 J. Wei, H. Zhu, Y. Jia, Q. Shu, C. Li, K. Wang, B. Wei, Y. Zhu, Z. Wang, J. Luo, W. Liu and D. Wu, *Carbon*, 2007, **45**, 2152–2158.
230 S.-H. Lee, J. Park, H.-R. Kim, J. Lee and K.-H. Lee, *RSC Adv.*, 2015, **5**, 41894–41900.
231 Z. M. Sheng, N. N. Li, Q. M. Xu, C. Y. Hong, S. Y. Wu, C. K. Chang, S. Han and C. M. Li, *Sustainable Energy Fuels*, 2021, **5**, 4080–4086.
232 Z. M. Sheng, C. Y. Hong, N. N. Li, Q. Z. Chen, R. P. Jia, D. Y. Zhang and S. Han, *Electrochim. Acta*, 2018, **259**, 1104–1109.
233 R. S. Wagner and W. C. Ellis, *Appl. Phys. Lett.*, 1964, **4**, 89–90.
234 G. J. Long and H. P. Leighly, *J. Chem. Educ.*, 1982, **59**, 948–953.
235 O. P. Krivoruchko and V. I. Zaikovskii, *Mendeleev Commun.*, 1998, **3**, 97–99.
236 A. R. Harutyunyan, T. Tokune and E. Mora, *Appl. Phys. Lett.*, 2005, **87**, 051919.
237 M. Takagi, *J. Phys. Soc. Jpn.*, 1954, **9**, 359–363.
238 F. Ding, A. Rosen and K. Bolton, *Carbon*, 2005, **43**, 2215–2217.
239 F. Ding, K. Bolton and A. Rosen, *Eur. Phys. J. D*, 2005, **34**, 275–277.
240 F. Ding, A. Rosen, S. Curtarolo and K. Bolton, *Appl. Phys. Lett.*, 2006, **88**, 133110.
241 F. Ding, A. Rosen, S. Curtarolo and K. Bolton, *Appl. Phys. Lett.*, 2006, **88**, 133110.
242 D. Schebarchov and S. C. Hendy, *Phys. Rev. B: Condens. Matter Mater. Phys.*, 2011, **84**, 085407.
243 E. Fitzer and S. Weisenburger, *Carbon*, 1974, **12**, 657–666.
244 M. S. Chambers, D. S. Keeble, D. Fletcher, J. A. Hriljac and Z. Schnepp, *Inorg. Chem.*, 2021, **60**, 7062–7069.
245 M. S. Chambers, R. D. Hunter, M. J. Hollamby, B. R. Pauw, A. J. Smith, T. Snow, A. E. Danks and Z. Schnepp, *Inorg. Chem.*, 2021, submitted.
246 H. Marsh and A. P. Warburton, *Carbon*, 1976, **14**, 47–52.
247 S. A. Steiner, T. F. Baumann, B. C. Bayer, R. Blume, M. A. Worsley, W. J. MoberlyChan, E. L. Shaw, R. Schlögl, A. J. Hart, S. Hofmann and B. L. Wardle, *J. Am. Chem. Soc.*, 2009, **131**, 12144–12154.
248 P. Xiao, Y. Gong, D. Li and Z. Li, *Microporous Mesoporous Mater.*, 2021, **323**, 111201.
249 F. J. Maldonado-Hódar, C. Moreno-Castilla, J. Rivera-Utrilla, Y. Hanzawa and Y. Yamada, *Langmuir*, 2000, **16**, 4367–4373.
250 C. J. Thambiliyagodage, S. Ulrich, P. T. Araujo and M. G. Bakker, *Carbon*, 2018, **134**, 452–463.
251 M. Sevilla and A. B. Fuertes, *Carbon*, 2013, **56**, 155–166.
252 F. Yu, J. N. Wang, Z. M. Sheng and L. F. Su, *Carbon*, 2005, **43**, 3018–3021.
253 H. Baker, *ASM Handbook: Alloy Phase Diagrams*, 1998, vol. 3.
254 R. Wang, G. Lu, W. Qiao and J. Yu, *Langmuir*, 2016, **32**, 8583–8592.
255 S. Yi, Z. Fan, C. Wu and J. Chen, *Carbon*, 2008, **46**, 378–380.
256 L. Zhao, X. Zhao, L. T. Burke, J. C. Bennett, R. A. Dunlap and M. N. Obrovac, *ChemSusChem*, 2017, **10**, 3409–3418.

